Geothermics 96 (2021) 102192

Contents lists available at ScienceDirect

Geothermics

journal homepage: www.elsevier.com/locate/geothermics

"Noise" during long-term continuous magnetotelluric monitoring of RN-15/IDDP-2 well engineering (Reykjanes peninsular, Iceland): A geogenic origin?

N. Haaf [a,b,*], E. Schill [a,b]

[a] Institute for Nuclear Waste Disposal, Karlsruhe Institute of Technology, Hermann-von-Helmholtz-Platz 1, 76344 Eggenstein-Leopoldshafen, Germany
[b] Institute of Applied Geoscience, Technische Universität Darmstadt, Schnittspahnstraße 9, 64287 Darmstadt, Germany

ARTICLE INFO

Keywords:
EGS
Magnetotelluric
Stimulation
Monitoring
Reykjanes

ABSTRACT

To date, magnetotelluric monitoring of processes during reservoir engineering of geothermal systems have been carried out only at three sites world-wide. Here, we add a new survey at the Reykjanes peninsular (Iceland). The MT data acquisition at RN-15/IDDP-2 covered the last third of the drilling period and thermo-hydraulic stimulation. Drilling was accompanied by temporal total fluid losses of up to 60 L/s as well as randomly distributed induced seismicity. Our experimental results of a two-months magnetotelluric monitoring during the deepening of the RN-15/IDDP-2 well on the Reykjanes peninsular (Iceland) to 4'659 m are in line with earlier observations on decreasing resistivities at periods of a few s to about 20 s (or up to about 40 s) in conjunction with fluid injection. Simple models indicate however that it is not the fluid volume itself that causes the anomaly. Moreover, here, temporal decreases in the electric resistivities occur at 0.2-20 s with minima at periods of about 0.4 s 1-2 days ahead of clusters of seismic events with magnitudes up to $M_L < 2$. Unlike in the previous studies, where resistivity decreases occur on the component that is parallel to Shmin, here they in both components (XY and YX) of the MT data. At the Reykjanes peninsular, Shmin is oriented N120°E off the XY component (N0°E). Therefore, if we rotate our data in Shmin direction, the difference between both components would be slightly smaller than that for the non-rotated ones. The decrease in resistivity (on both components) extends over > 1 order of magnitudes over a short period range and is thus considered noise induced in the subsurface. This study aims at adding an essential dataset to the general discussion on MT monitoring of reservoir processes. The results show a temporal relation between decreasing apparent resistivity and (i) the geomagnetic field activity, (ii) the fluid losses up to 60 L/s, as well as (iii) mechanic processes occurring in the reservoir before clusters of induced seismicity on the other hand.

1. Introduction

Enhanced geothermal systems (EGS) in fractured reservoirs are typically engineered by hydraulic stimulation (Häring et al. 2008; Baisch et al. 2006; Baisch et al. 2010; Cuenot et al. 2008; Schill et al. 2017). In the past, these measures were often accompanied by sensible induced seismicity (Häring et al. 2008; Baisch et al. 2006; Baisch et al. 2010; Cuenot et al. 2008; Schill et al. 2017). Subject matter of current EGS research is, therefore, the mitigation of induced seismicity. New hydraulic stimulation schemes led to full mitigation of sensible induced seismicity (e.g., Baujard et al. 2017). Since induced seismicity is also used for monitoring of dynamic processes during hydraulic stimulation, upon its mitigation, the development of new monitoring techniques is of interest.

Marquis et al. (2002) and Darnet (2004) report significant increase in electric self-potential with fluid injection into the EGS reservoir at Soultz-sous-Forêts. Moreover, a second increase in self-potential is observed during the so-called shut-in phase, in which the seismic energy release increases significantly as well (Schoenball et al. 2014). Recent studies extend such observations during injection to the electric and magnetic properties of the subsurface. The first successful applications of MT monitoring were obtained at the Paralana and Habanero EGS sites (Peacock et al. 2012; Peacock et al. 2013; Didana et al. 2017) and the Rittershoffen site (Abdelfettah et al. 2018). A compilation of the boundary condition and observations is provided in Table 1.

At Paralana, micro-seismicity and MT monitoring was carried out

* Corresponding author.

https://doi.org/10.1016/j.geothermics.2021.102192
Received 16 April 2020; Received in revised form 31 May 2021; Accepted 22 June 2021
Available online 2 August 2021

Table 1
Summary of the tectonic boundary condition and electromagnetic observations during injection experiments in EGS wells (Peacock et al. 2012; Peacock et al. 2013; Didana et al. 2017; Abdelfettah et al. 2018; Baujard et al. 2017).

Orientation of \ Site	Paralana	Habanero	Rittershoffen
SHmax	N110°E	N82±5°E	N170°E
Seismic cloud	NNE-SSW, NE-SW	Horizontally extended with tendency to N-S, NNE-SSW orientation	n/a
Geoelectric strike	N9°E	N50°E	N-S
Resistivity of injected fluid	0.3 Ωm	13 Ωm	0.15 Ωm
Residual phase tensor during injection	N-S, NNE-SSW	N-S	N170°E
Electromagnetic component revealing significant resistivity minima	XY ∥ N-S	XY ∥ N-S	YX ∥ E-W

during a four days injection of 3'100 m^3 of saline water into the Paralana-2 well at 3'680 m depth at injection rates up to 58 L/s and well-head pressures up to 62 MPa. The resulting residual phase tensor ellipses of MT data between pre- and post-stimulation are oriented N/NNE-S/SSW coinciding with one of the two pre-existing fracture families obtained from micro-seismic analyses, with the regional electric strike and being sub-perpendicular to the maximum horizontal stress (SHmax). Compared to pre-injection electric resistivity, the post-injection values reveal a decrease in resistivity in the XY component from periods of 2 s and reaching up to 20 Ωm at periods of 20 s which corresponds to the orientation of the minimum horizontal stress (Shmin), the geoelectric strike, and the natural and residual phase tensors. The micro-seismicity concentrates NE of the borehole with an overall alignment NE-SW direction. However, two branches of the seismic cloud develop in approximately N-S direction parallel to the XY-component (Albaric et al. 2014). Note that changes on the YX component are by one order of magnitude smaller (Peacock et al. 2012; Peacock et al. 2013).

At the Habanero-4 well, a volume of 36'500 m^3 was injected at up to 53 L/s and up to 48 MPa (Didana et al. 2017). Here, residual phase tensor ellipses are oriented approximately N-S sub-parallel to the tendency of horizontal development of the seismic clouds and sub-perpendicular to SHmax. Changes in apparent resistivity occur at periods of 17 to 34 s and aligning along a N-S direction that is parallel to Shmin.

First long-term MT monitoring of EGS was carried out during a period of about five month by Abdelfettah et al. (2018). This period covers different intervals of fluid injection and production in the two wells GRT-1 and GRT-2. The fluid injection was accomplished at low volumes and low flow-rates at maximum values of 28 L/s (GRT1) and 42 L/s (GRT2), and low well-head pressure of 1-3 MPa (Abdelfettah et al. 2018; Baujard et al. 2017). Comparable to the results at Paralana and

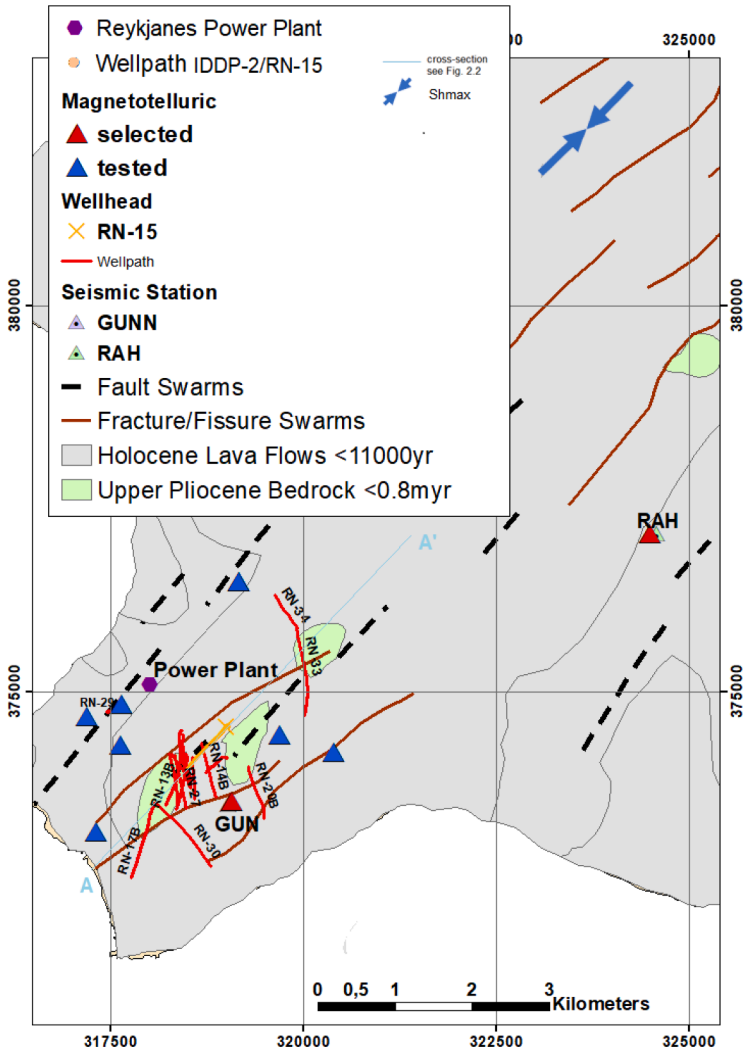

Fig. 1. Experimental and geological setting of the MT monitoring of the well RN15/IDDP-2 including the MT stations, the wellhead (modified after Johannesson and Sæmundsson (2009)).

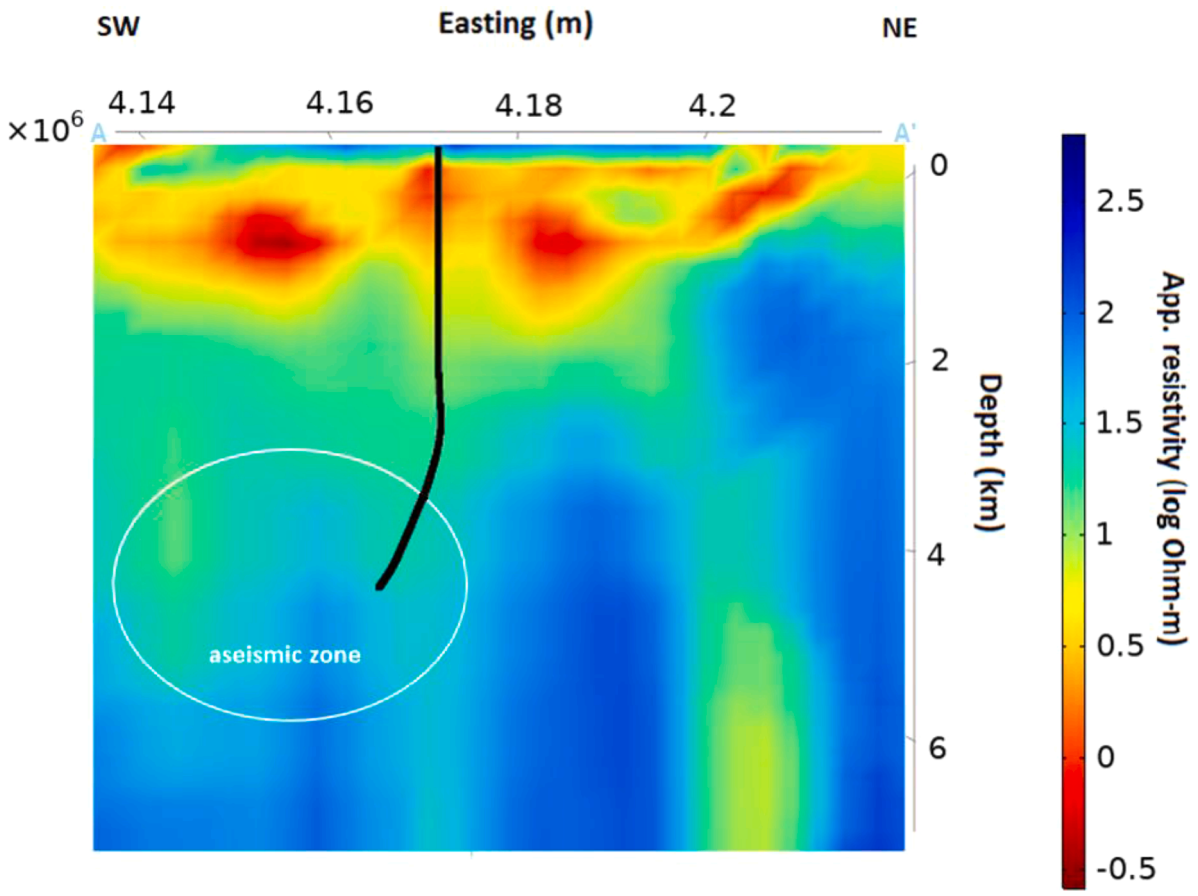

Fig. 2. 3-D MT inversion profiles from NE to SW and NW to SE (Karlsdóttir and Vilhjálmsson 2016).

Habanero, the results reveal resistivity decreases from about 1 to 0.1 Ωm in the components with a preferential direction sub-parallel to Shmin. Note that this effect is observed during injection, but not during production.

This directional particularity and the occurrence of resistivity decrease during injection, only, point to effects beyond electro-kinetics. Possible seismo-electric or -electromagnetic phenomena are a matter of research. Although the source of the mechanical disturbance that activates seismo-electromagnetic effects may be distant, Gershenzon and Bambakidis(2001) assume that the source of the electromagnetic signal itself is local. In this context, in the last decades seismo-electromagnetic phenomena were interpreted as possible precursors for earthquakes. Petraki et al. (2015) gave a summary of different kinds of electromagnetic anomalies in a wide frequency range from extremely low frequencies (ELF at 1-300 Hz) to high frequencies (HF at 3-30 MHz). Ohta et al. (2013), for example, measured increased magnetic field changes (H, D, and Z components) in the ULF/ELF frequency range five days before the Tohoku earthquake, Japan, on March 11, 2011 using three orthogonal magnetometers in the frequency range of 0.1-24 Hz. Such effects are approached in lab experiments (e.g. Freund 2011), but to date are not fully experimentally verified.

A crucial discussion in this respect is the distinction between transient effects in the electric and magnetic field of the subsurface caused by injection or seismicity from other uncorrelated noise in the MT data. Hereby, it must be considered that if the duration of the perturbation underruns the measurement window, by definition it contributes to the uncorrelated noise. Generally in MT, noise is defined as the part of a dataset that cannot be explained by theory (Junge 1996). The literature distinguishes between geological, cultural, and instrumental noise in electromagnetic data (Chave and Jones 2012; Junge 1996). In conventional MT, remote referencing (Gamble et al. 1979; Clarke et al. 1983) is used to eliminate uncorrelated noise from measured data. In the vicinity of geothermal drilling, electric pumps, power lines, pipelines, or also mechanical vibration from heavy instruments can contribute to cultural noise. For reasons explained below, in this study, we define noise as a temporal variation of the EM field with a frequency higher than the processing window.

In the following, we present the results of MT monitoring during deepening the well RN-15/IDDP-2 located on Reykjanes peninsular that was carried out together with the time-lapse CSEM survey (Darnet et al. 2020). In the latter a high CSEM survey repeatability was achieved with electric field measurements (within a few percent). Time-lapse MT survey was classified a challenging task because of the high level of noise. The continuous MT monitoring covered the last third of the drilling period. During this period, injection rates of up to 115 L/s were reached. Furthermore, this period of the drilling operation was accompanied by induced seismic events with magnitudes up to 1.7.

2. Geophysical setting and well path

The MT monitoring is set-up around the well RN-15/IDDP-2 of the Reykjanes geothermal field (Fig. 1). With the aim to establish injection underneath the conventional geothermal system to support productivity, this well was deepened from 2'500 to 4'659 m measured depth (MD) between 08/2016-01/2017 in the framework of the H2020 DEEPEGS project (www.deepegs.eu). Being inclined by about 40° towards N220°E from 2'750 m downwards, the well reaches a true vertical depth (TVD) of 4'469 m and its bottom hole locates at 738 m beeline SW of the wellhead position.

The Reykjanes peninsular represents the continuation of the mid-Atlantic ridge above sea level and is characterized by a rift zone with active volcanoes as well as fault and fracture swarms that are oriented

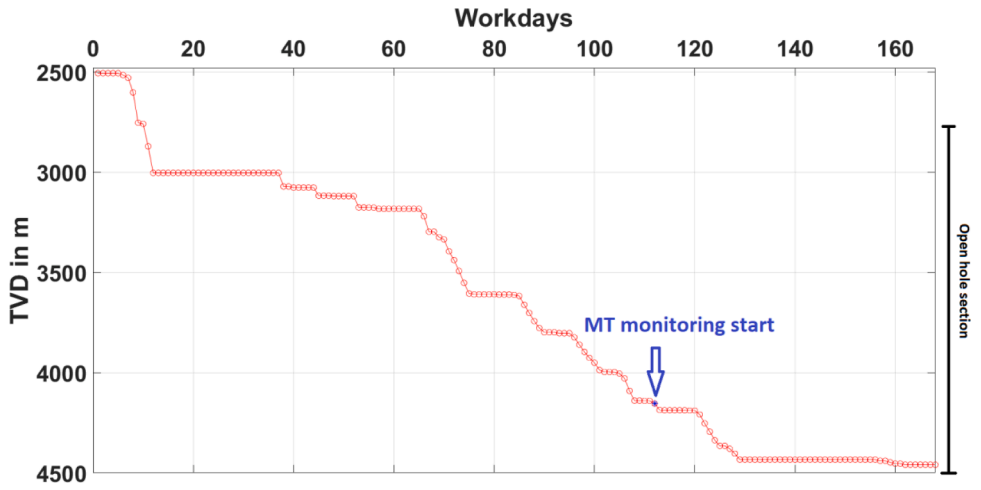

Fig. 3. The daily drilling progress of RN-15/IDDP-2 deepening with the workday 1-168 on 11/08/2016-25/01/2017 (data provided by HS Orka hf (2017). Start of MT monitoring: workday 112 (30/11/2016) is marked with the blue circle and arrow.

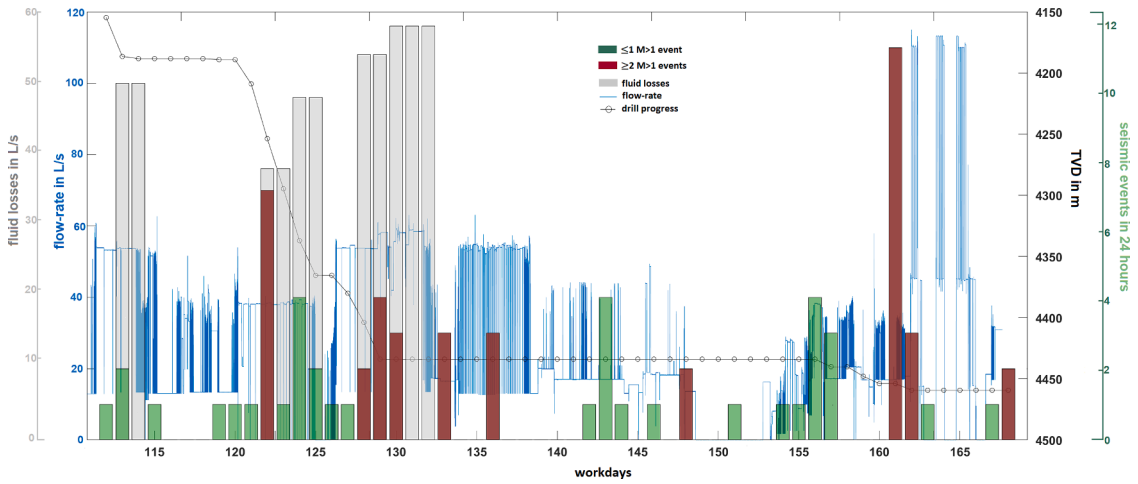

Fig. 4. Injection rates into RN15/IDDP-2 (blue lines, HS Orka hf (2017)), total or nearly total fluid losses in 24-hour windows (yellow, Weisenberger et al. (2017), and induced seismicity in 24-hour windows (green and red, modified after Gaucher, pers. comm.) during the MT monitoring from 30/11/2016-26/01/2017.

approximately NE-SW. The state of stress of the Reykjanes peninsular was estimated by inversion of micro-earthquake focal mechanisms. It is mainly oblique strike slip, with a tendency towards a normal stress state. The average Shmin direction of N120±6°E is in agreement with the directions of greatest extensional strain rate derived from GPS velocities (Keiding et al. 2009).

Inversion of MT data from the Reykjanes field (Karlsdóttir and Vilhjálmsson 2016) reveals a typical resistivity structure of a high-temperature geothermal system with a low resistivity cap layer covering the conventional geothermal field in this area (Fig. 2). Below this feature, a sequence of alternating resistivities with minima of about 10 and maxima of about 100 Ωm extend vertically to the bottom of the model. These structures have been attributed to a dyke swarm or a sheeted dyke complex (Friðleifsson et al. 2014).

Note that the RN-15/IDDP-2 well has been extended into a formerly aseismic zone with a vertical extension of about 3-6 km depth (Guðnason et al. 2015). The seismic activation of this zone at about 3-4.5 km depth occurred principally during deepening of RN-15/IDDP-2 starting in 08/2016 (Guðnason et al. 2016). During the entire drilling period (08/2016 to 01/2017), a number of 357 earthquakes with magnitudes between 0.5 to 2.0 occurred in the depth range of 2-5 km close to the borehole. Increasing depth of the hypocenters is attributed to the drilling progress. Interestingly, the above mentioned alternating resistivities occur only below this aseismic zone. For comparison with processes on-going in the reservoir and surroundings during the MT monitoring period, in addition to the seismic network SIL of the Iceland Geo Survey (ISOR, in operation since 2013), the data from a local seismic network that was installed in the vicinity of the well (HS Orka hf 2017) are used.

The complete deepening progress of RN-15/IDDP-2 (Friðleifsson et al. 2017) is shown in Fig. 3. A production casing was installed down to 2'941.4 m MD (2'939.4 m TVD) on the workdays 1-37 (Weisenberger et al. 2017) (Fig. 3). The MT monitoring started during drilling on workday 112 at a borehole depth of 4'271 m MD (4'154.7 m TVD). Drilling to 4'310 m MD (4'188 m TVD) and reaming of this section was terminated on workday 116 and followed by logging and coring. Drilling to 4'626 m MD (4'434 m TVD) and reaming is resumed on workdays 121-132. At this depth, on workdays 133 et seqq., testing is followed by logging and casing setting. Cementing of the perforated liner was carried out on workdays 149-152. Drilling is resumed on workday 155. The final depth of 4'659 m MD is reached on workday 162. Between workdays 163 and 166, thermal and hydraulic stimulation of the perforated and the 1'778.8 m long open hole section is carried out.

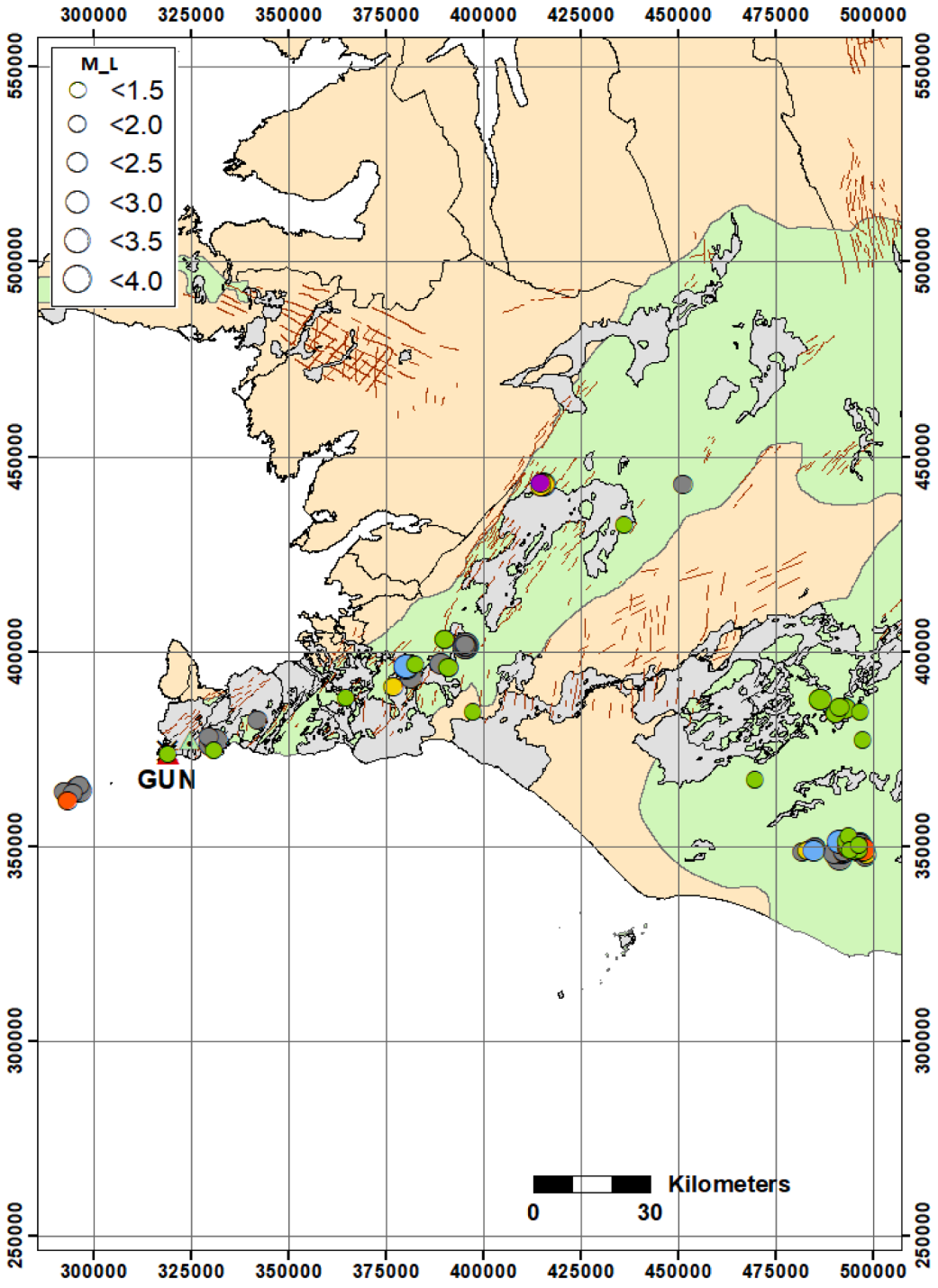

Fig. 5. Local and regional seismicity on the Reykjanes peninsular (M_L>1.66) during the MT monitoring period 30/11/2016-26/01/2017 and seismic events with M_L < 4.0 from the SIL network (Icelandic Meteorological Office 2017). The events of case 1 are plotted in yellow, case 2 in orange, case 3 in violet, case 4 in blue, case 5 in green and all events not related to the cases in grey. The size of the circles corresponds to the magnitude ranges.

3. Hydraulic and seismic observations during drilling and stimulation

Hydraulic and seismic observations during MT monitoring, i.e. during drilling (workdays 112-163) and hydraulic stimulation (workdays 164-169), are summarized in Fig. 3. Until workday 116 (drilling and reaming down to 4'310 m MD), the injection rates vary between 15-54 L/ s. The next section down to 4'537 m MD is drilled at injection rates of 0-40 L/s (workdays 121-126). Between workdays 127-129, the well reaches 4'626 m MD and fluid is injected with 15-54 L/s followed by 58 L/s. During logging (workdays 135-140), injection rates of 15-54 L/s are used. The final section down to 4'659 m MD is drilled at increasing injection rate ranges from a few L/s to 30 L/s to 20-40 L/s (workdays 155-164).

Thermal cycling and pressurization were performed to improve the injectivity of the well. In short steps, the injection rates were raised to 110-115 L/s via rig pumps and then decreased to zero for a quick warm-up. The results indicate that the injectivity for the well improved considerably from 1.7 L/s/bar at the end of the drilling to 2.9 L/s/bar during the stimulation and to 3.1 L/s/bar at the end of this stimulation

Table 2
Summary of the parameter that were applied during data processing using the advanced mode in BIRRP (Chave and Thomson 2003, 2004).

Parameter	Value
Time-bandwidth for the Slepian data taper	2
Maximum FFT section length	1'024
Total number of reductions	6
Factor of section reduction	2
Index of the first frequency in each section	8
Increment of the first frequency in each section	1
Number of frequencies	8
Coherency threshold for the vertical magnetic field	0.5
Length of time windows of two consecutive days	524'288 points
Number of frequencies to be rejected	2
Pre-whitening filter order	5

stage (Sigurðsson 2018).

Note that all experiments were carried out using freshwater at a conductivity of 15'120 μS/cm from a groundwater well at a distance of about > 1.5 km from the drill site. This translates to a fluid resistivity of about 0.66 Ωm. In case the injected volume would be large enough to cause any effect on the bulk resistivity, injection into the present matrix with a resistivity of 10-100 Ωm (Fig. 2) would result in a no or an only a slight change in the decrease in resistivity.

During drilling, total or nearly total fluid losses occurred during the workdays 113-114, 122-125, and 128-132. The latter two are linked to the occurrence of induced seismicity with magnitudes reaching up to M = 1.7.

The number of seismic events in 24-hour windows distinguishing between windows with two or more events with a magnitude M > 1 (red in Fig. 4) and windows with one or less events of this size (green in Fig. 4) reveals maximum seismic activity during the MT monitoring

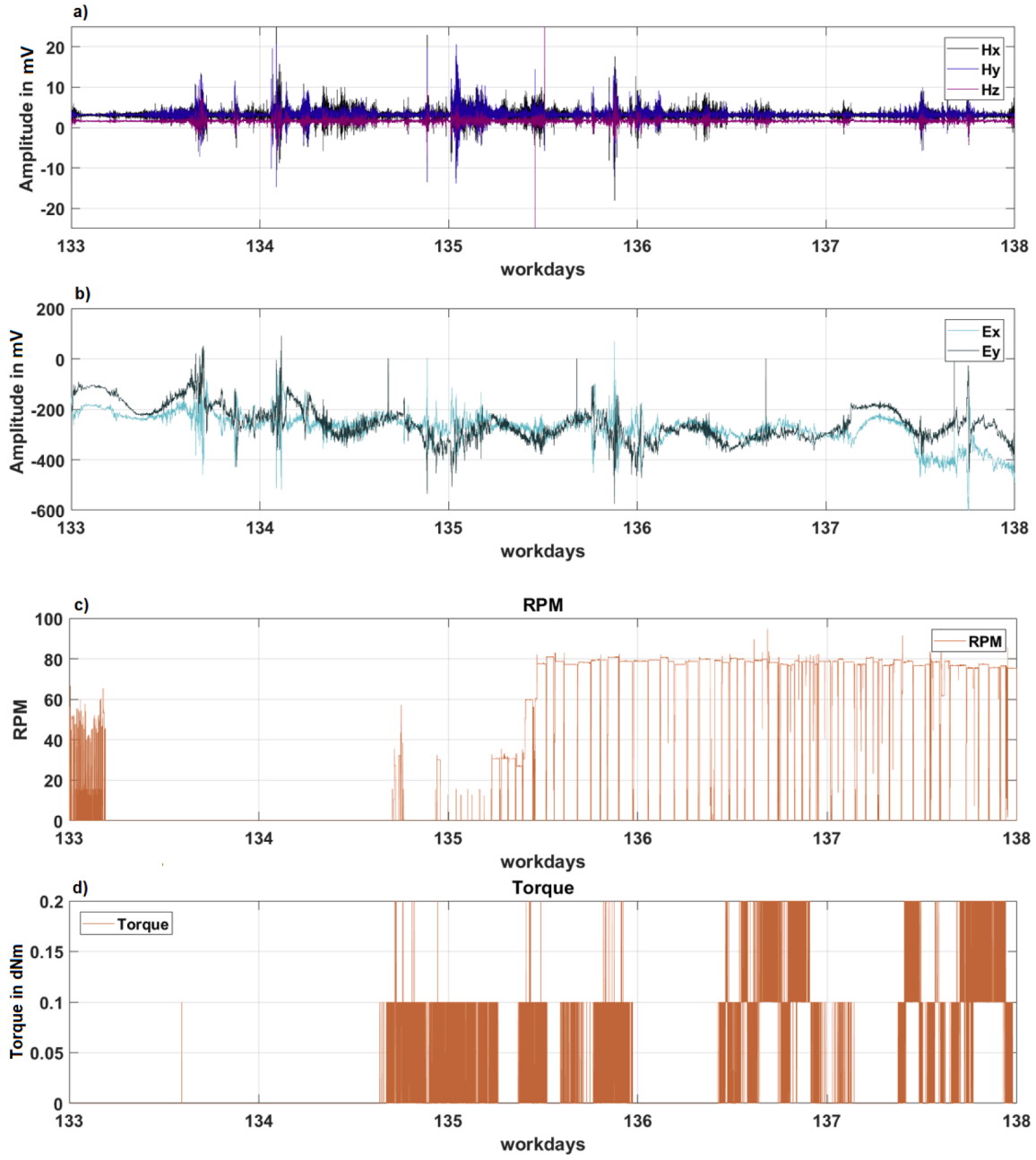

Fig. 6. a) The magnetic field components, H_x, H_x, and H_z, b) the horizontal electric field components, E_x and E_y, and c) the rotation speed in revolutions per minute (RPM) and the torque (dNm) for the workdays 133-138 (HS Orka hf 2017).

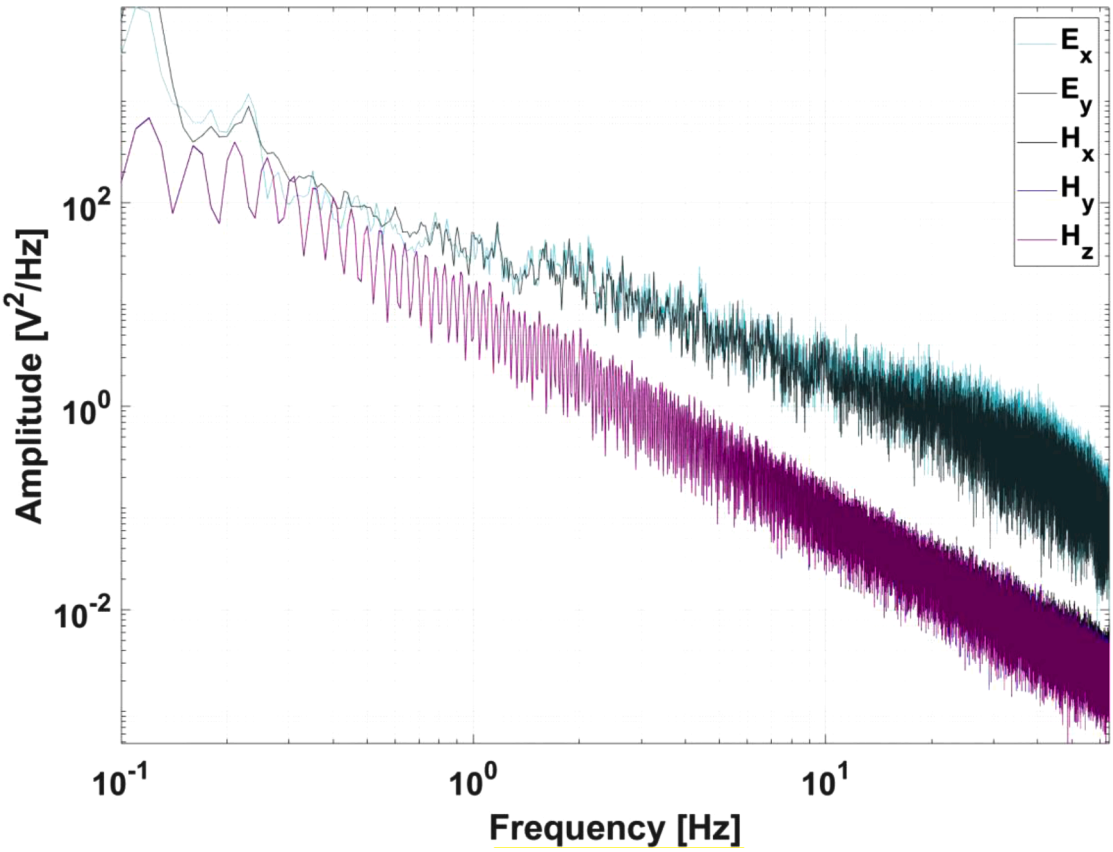

Fig. 7. A representative calculated power spectra for the time series recorded during workdays 133-137.

period on workday 161 with eleven events followed by seven events on workday 122, both days with at least two events with M > 1. On workday 122 drilling was resumed at injection rates up to 40 L/s. The next period of important seismicity started on workday 128 and lasted until 136. This phase corresponds to comparatively high injection rates of up to 58 L/s and moreover relatively high lower limits of up to > 40 L/s. During the period of maximum seismic activity, injection reach a local maximum of 40 L/s. Interestingly, during the hydraulic stimulation significant seismic activity occurs only at the beginning of the third of three injection cycles.

In Fig. 5, we provide an overview of the local (see Fig. 4) and the regional seismicity in Iceland (Icelandic Meteorological Office 2017). During the MT monitoring period, regional seismicity in SW-Iceland reveals seismic events with magnitudes of up to $M_L = 3.6$. Note, that the events are clustered in workday intervals in Fig. 5. This step provides a better basis for the following sections and discussion. Case 1 includes the workdays 157-163 in yellow, case 2 112-115 in blue, case 3 133-137 in violet, case 4 126-130 in orange, case 5 136-143 in green and all event outside of these intervals are plotted as grey circles. The magnitude defines the size of the circles. Several regional events exceed the local magnitude of $M_L = 1.7$ (see Fig. 4).

4. Experimental setup and data processing

4.1. MT Experimental setup

In a first field campaign in 09/2016, eight stations were tested concerning the expected electric noise to identify an optimal location for continuous MT monitoring (Darnet et al. 2020). Based on the relatively high signal-to-noise ratio, as well as for practical operation and maintenance regarding power supply and data transfer and reasons for data comparability, the two continuous monitoring stations, GUN and RAH, were selected close to the equally named seismic stations (Fig. 4). The GUN station represents the main monitoring site and is located about 750 m S of the wellhead of RN-15/IDDP-2 well and about 700 m to the SE of the projection of the bottom of the well at the surface. The RAH station is located at about 5 km NE of the wellhead. RAH was planned to operate as a second continuous monitoring station with the potential of being a local remote reference. To measure orthogonal and time-dependent components of the Earth's magnetic field and the corresponding electric response, both stations were equipped with a battery-powered Metronix controlling unit ADU-07e, EFP-06 electrodes and MFS-07e broadband induction coil magnetometer. The electric dipole lengths were 100 m in N-S and E-W direction. The contact resistance of the electrodes was < 2000 Ωm and loggers and cables were buried to about 10 cm depth to protect them from the weather. Data collection and station maintenance was carried out by the Iceland Geological Survey ISOR at a frequency of 1-2 weeks. At GUN, continuous monitoring was carried out between 30/11/2016 and 21/07/2017 in 24-hour periods using a sampling frequency of 512 Hz. Due to failure of the data logger, continuous data coverage lags at GUN during the workdays 117-119, 145-152, 155, 158, 161, and 164. Measurements at RAH were stopped in 05/2017 due to continuing bad data quality after mid of 12/2016.

4.2. Data processing

The data were processed using the bounded influence remote reference processing software BIRRP (Chave and Thomson 2003, 2004) in the so-called advanced mode that requires remote referencing. The processing included a full impedance tensor analysis. To overcome the absence of high quality remote data (see below), the station data itself were used also as remote reference. To obtain the best possible data quality and low error bars, the following parameters were selected from

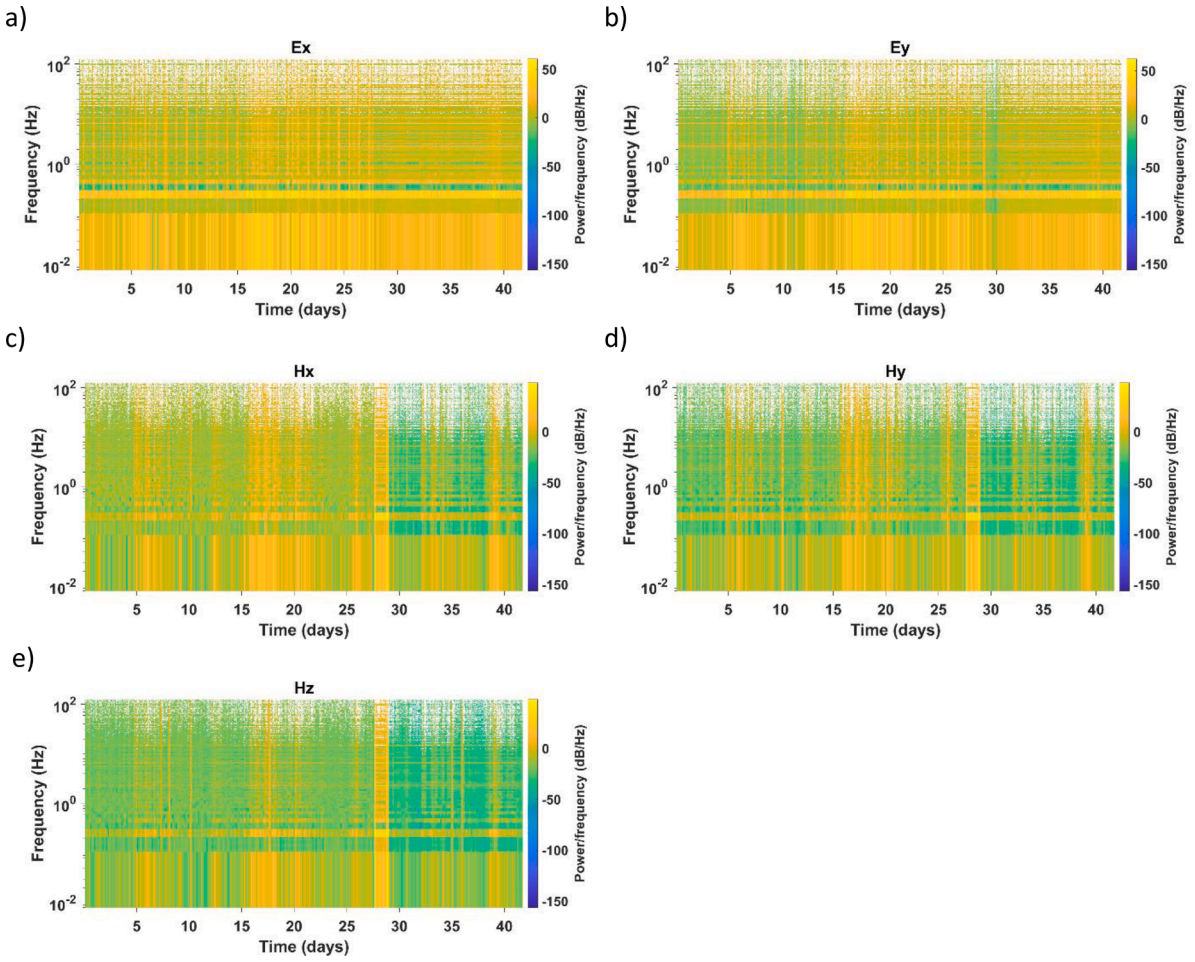

Fig. 8. Spectrograms of the time series (a) Ex, (b) Ey, (c) Hx, (d) Hy and (e) Hz with 3600 s window lengths and 50 % overlap.

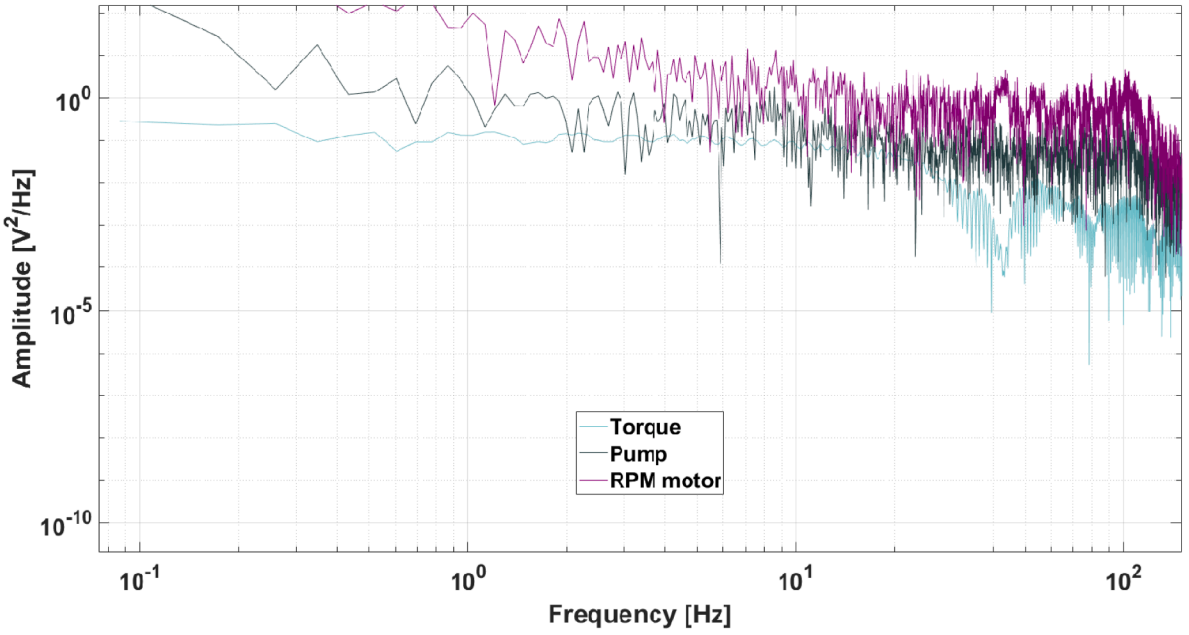

Fig. 9. Power spectral density of torque, RPM with motor and flow-rate.

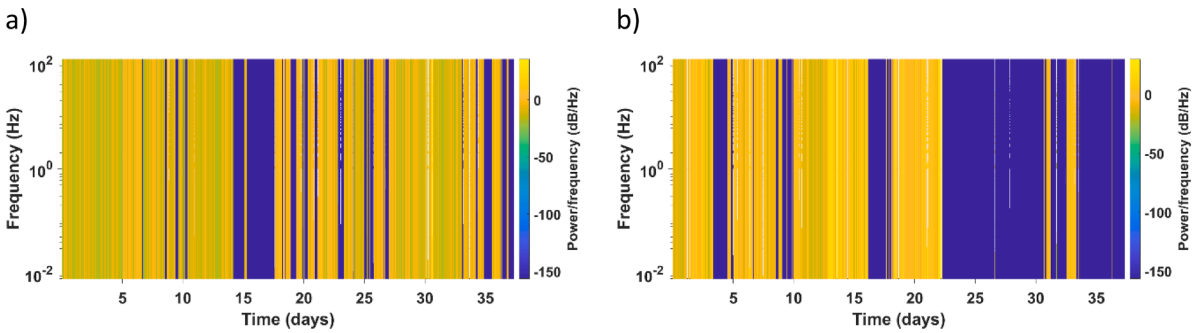

Fig. 10. Cross-spectrogram of (a) Ey and torque and (b) Hz and RPM.

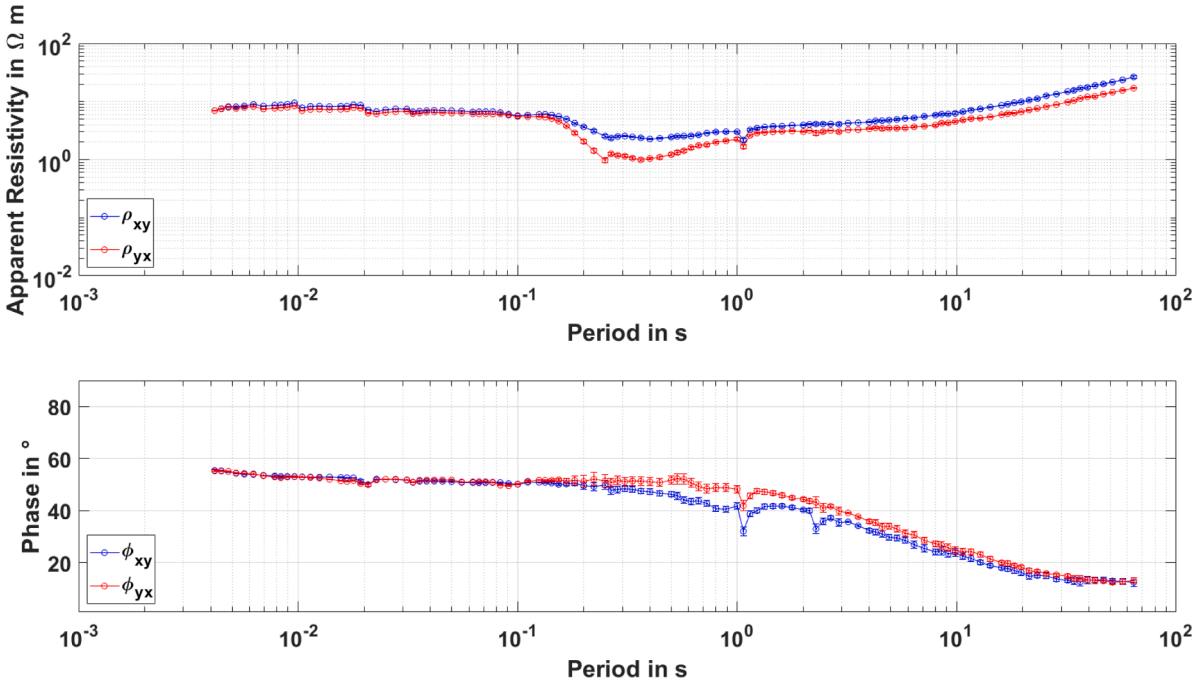

Fig. 11. Single-site processed, filtered and decimated from 512 to 128 samples/s reference transfer function (workdays 46-47) with a) resistivity and b) corresponding phase.

Table 3
Overview of the changes in the geo-magnetic field activity, the induced seismicity and fluid losses occurring during the workdays of the cases 1 to 4 (including data gaps of MT monitoring).

	Case 1	Case 2	Case 3	Case 4
Workdays	157-163	112-115	133-137	126-130
Total fluid loss during seismicity events	-	> 50 L/s on workdays 113-114	-	> 54 L/s on workdays 128-132
Number of induced seismic events	15 on workdays 161-163	2 on workday 113	6 on workdays 133 and 136	11 (9 on workdays 128-130)
Maximum magnitude	1.25	1.23	1.66 on workday 133	1.44
Workdays with Ap < median value	157-160	112-115	-	126-128
MT data gap	161	-	-	-

test runs (Table 2).

A notch filter of 50 Hz was applied before processing. The transfer functions are averaged over 48 hours to obtain a reasonable resolution for the depth of investigation. In the following, the off-diagonal components are displayed, since diagonal components' values are typically close to zero. The data uncertainties in the transfer functions were computed using the robust statistical Jackknife approach (Chave and Thomson 2003). The resulting overall data quality is moderate to good. Note that the quality of data strongly decreases in the near surface periods down to a few 10^{-2} s.

Remote referencing was tested using the data from 09/2016 together with a station at intermediate distance at 46 km (at X=363'000 and Y = 389'600 in Fig. 5). Error bars in the transfer functions are not decreased by remote referencing but smoothing of the transfer functions is achieved. Due to weather condition, this remote station can be operated only in summer. Therefore, the RAH station was installed during wintertime. However, remote referencing was not applicable throughout the monitoring period due to the bad data quality at RAH and the Wittstock stations (Ritter et al. 2015). The closest geomagnetic observatories of the INTERMAGNET (www.intermagnet.org) are Lerwick and Narsarsuaq. However, data at these stations are acquired at a sampling rate of 1 Hz; to use these stations as remote reference would require deleting more than 99% of our data. Moreover, MT monitoring aims at observing changes in the electromagnetic field triggered by the hydraulic load in the reservoir. When cross-powers between the remote

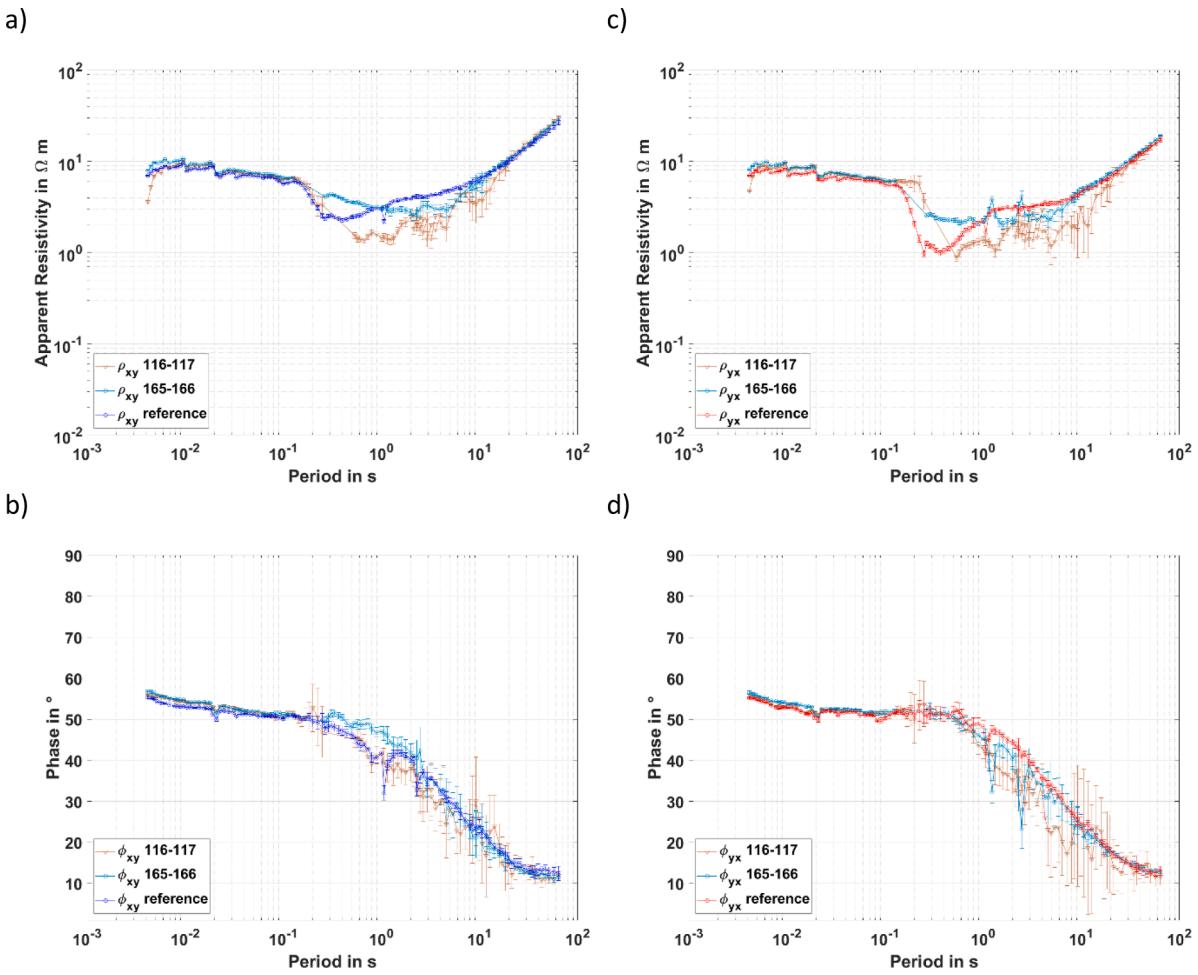

Fig. 12. Transfer functions of the workdays 116-117 and 165-166 (injection rates of 15-54 L/s and in the latter 0-115 L/s) with a) apparent resistivity, and b) phase of the XY component.

and local variables rigorously replace the local auto- and cross-powers, the high-frequent target signal of MT monitoring may be removed because it appears as uncorrelated noise (Chave and Jones 2012).

For these technical and conceptual reasons, the single-site processing appears to be the best compromise for this survey. To eliminate only the uncorrelated noise that originates from operations at the surface, we applied notch filters of the respective frequencies. In the case of the high-frequency signal, an improvement of filtering is achieved by the decimation of the sampling frequency before filtering.

Note that a geoelectric strike of N0°E is derived after Becken and Burkhardt (2004). Given our experimental setting, no rotation of the impedance tensor is required for further analyses. Thus, XY- and YX-components are sub-parallel to N-S and E-W directions, respectively.

5. Analyses of transient effects

5.1. Time-frequency analyses of anthropogenic noise sources

In the following, we provide time series and power spectra of representative workdays to elucidate the noise and a possible influence of the drilling process on the electromagnetic signal. As type parameter, we show the rotational speed of the drill bit and the torque, i.e. the rotational force between the drill string and the formation, compared to the magnetic and electric component for a representative time period (Fig. 6). Time series are generally noisy. The electric components seem to be affected by a periodic signal that corresponds to tidal noise periods (Fig. 6b). A clear correlation between noise and the onset of drilling is not evident.

The power spectra electric and magnetic components (Fig. 7) were calculated using Welch (1967). The magnetic components reveal similar distributions without visible peaks. The electric components show several but small peaks between 4-10 Hz that coincide with the Schumann resonances. Generally the magnetic components appear to be less affected by noise.

A time-frequency analysis allows for examining possible noise sources or frequencies. Fig. 8 shows the spectrograms of the time series of the five MT components at a window length of 3600 s and 50 % overlap that provides optimal resolution for both, time and frequency. Highest power-to-frequency occurs across the entire time period in the electric components for frequencies between 0.1-0.01 Hz, and high power-to-frequency between 10^2-1 Hz. Moderate power-to-frequency values are between 0.2-0.5 Hz in the dead band for all five channels. Compared to the electric, the magnetic components reveal rather moderate power-to-frequency values.

In order to investigate for periodic signals in the drilling parameters their power spectral density was estimated. Three representative parameters, RPM with additional motor, torque and pump are shown in Fig. 9. While all three spectra show maxima at $>$ 100 Hz, the torque reveals additional local minima at 40 and 80 Hz.

To identify anthropogenic noise from the drilling operation, for each time series the cross-spectrogram with each drilling parameter is calculated. The window lengths are 100 s and 50 % overlap considering the lower sampling rate of 0.2 Hz for the drilling parameters.

Fig. 10 shows exemplary the cross-spectrograms of Ey with torque

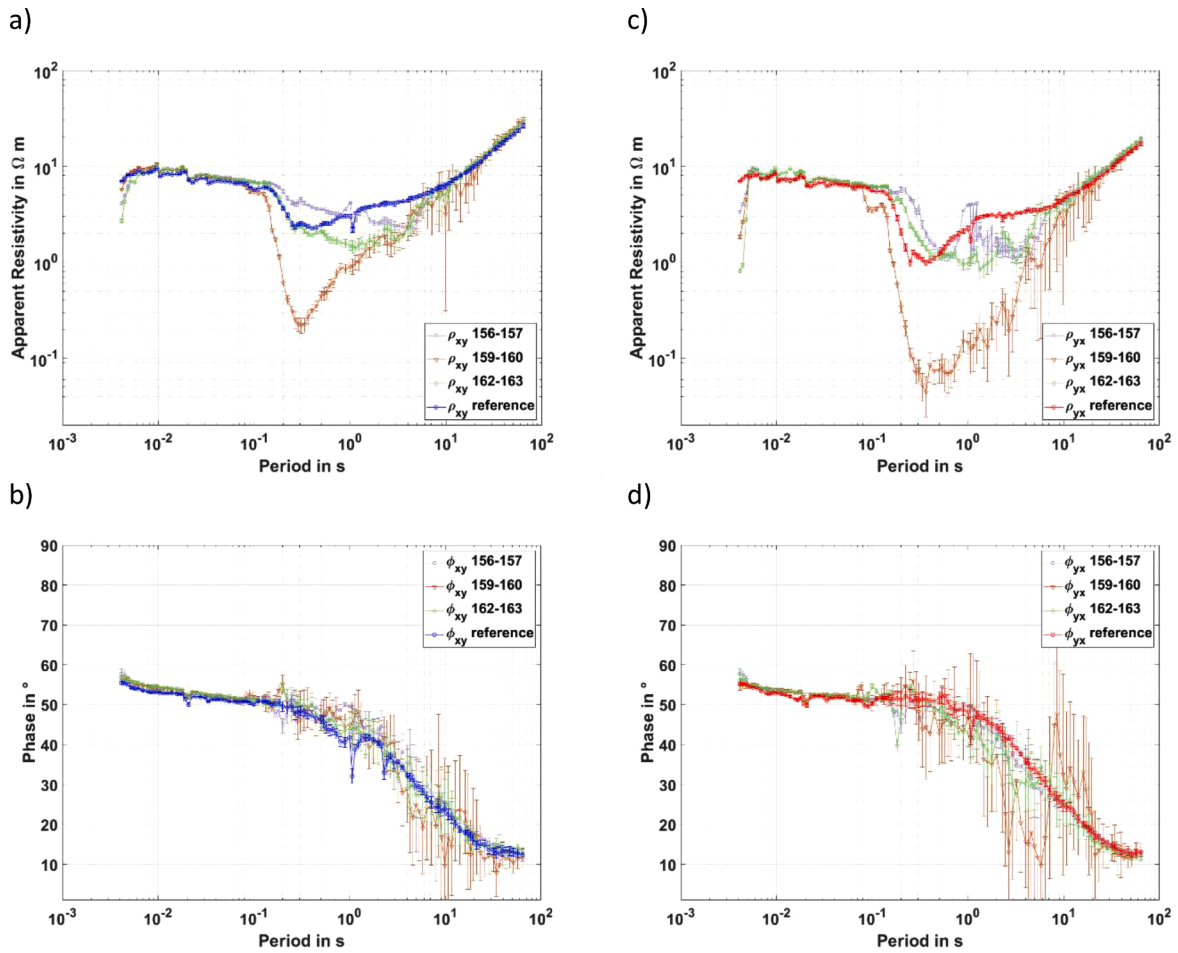

Fig. 13. Transfer functions of the workdays 157-163 before, during and after 15 induced seismic events for the XY-component with a) apparent resistivity, and b) phase, as well as the YX-component with c) apparent resistivity, and d) phases.

and Hz with RPM. As in Fig. 8 the sampling rates of 128 Hz and 0.2 Hz appear as high power-to frequency values. Since drilling parameters are controlled by the lithology and progress, vertical blocks of lowest power-to-frequency values of 160 dB/Hz appear at times when no torque or rotation speed is applied to the drilling equipment. In contrast to Fig. 6, the cross-spectrogram of Ey with both, torque and RMP (not shown) does not reveal periodic signals.. High power-to-frequency signals are observed throughout the monitoring period besides the periods when the drilling parameters are not used (blue colored).

To conclude, the drilling parameters and the MT time series do not show common periodic signals or events. The exception in the electric time series which may be attributed to tidal noise.

5.2. *Temporal changes in the transfer functions*

In the following, the resulting single-site processed, filtered and decimated transfer functions are averaged over 48 hours with an overlapping window of 24 hours. Since operation in the conventional field is continuously on-going and MT monitoring started during drilling, a reference day is required for comparison. To describe the geomagnetic activity, we use the A_p value, i.e. the daily average of the K_p-values (GFZ German Research Centre For Geosciences 2020). The daily values are compared to the median value of 5 over the entire measurement period of workdays 112 to 167.

5.2.1. *Reference transfer function and introduction to the cases*

Given the unexpected high fluid losses and the induced seismicity during the deepening phase of RN-15/IDDP-2 as well as the continuous operation in the conventional part of the Reykjanes geothermal field, monitoring was started already during this deepening period and thus, an unbiased reference could not been acquired. The reference transfer function that has been acquired during the workdays 46-47 (25-26/9/2016) is shown in Fig. 11. These two days have been chosen on the following criteria. The drilling had not yet reached the later openhole section. No drilling, but only cementing was ongoing.

The transfer function reveals a comparably smooth resistivity distribution with periods. Between 0.002 to 0.1 s, resistivity values are in the order of 10 Ωm with slightly decreasing tendency towards longer periods. A significant decrease to 1-3 Ωm, for the YX- and XY-components, respectively, is observed between 0.1-1 s. Towards longer periods, resistivity increases continuously. Generally, the YX-component reveals lower values. Note that the high geomagnetic activity during the workdays 46-47 is indicated by an Ap value of 20-22.

In the following, representative workday pairs with different combinations of geo-magnetic, hydraulic and seismic conditions are analyzed with respect to their electromagnetic responses. The following cases include relatively low geo-magnetic field activity, no circulation loss, small magnitudes and high numbers of events (Case 1), relatively low geo-magnetic field activity, total circulation loss, small magnitudes and low number of events (Case 2), relatively strong geo-magnetic field activity, no total circulation loss, large magnitudes and low number of events (Case 3), and relatively low geo-magnetic field activity, total circulation loss, intermediate magnitudes and high number of events (Case 4). An overview of the cases is given in Table 3.

During workdays without total fluid losses or significant seismicity, little variation from the reference transfer function is observed (Fig. 12).

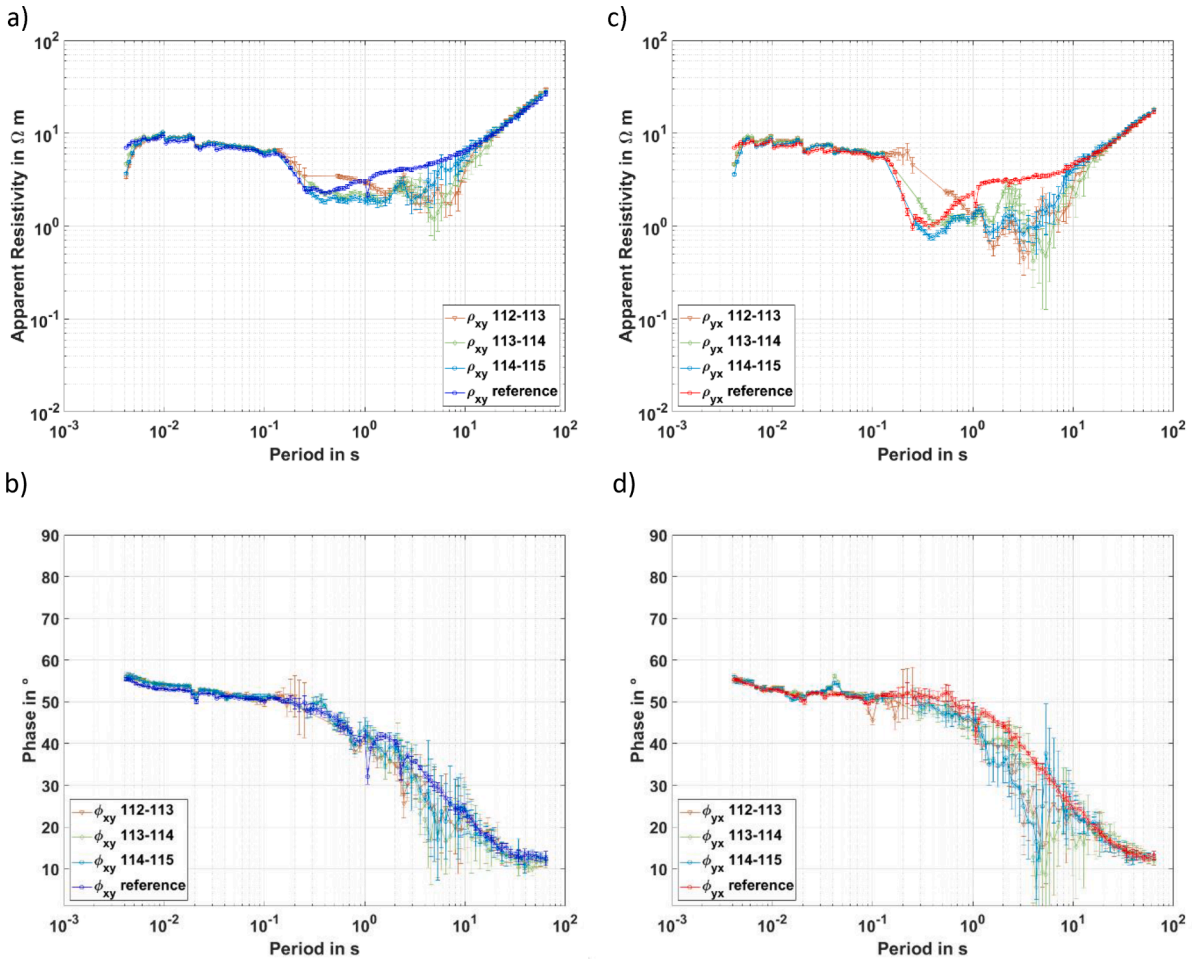

Fig. 14. Transfer functions of the workdays 113-114 during total fluid loss for the XY-component with a) apparent resistivity, and b) phase, as well as the YX-component with c) apparent resistivity, and d) phases.

During the representative workdays 116-117 and 165-166, 15-54 L/s and 0-115 L/s, respectively, were circulated at different frequencies. Note that during both periods geo-magnetic activity is low (Ap values < median value). The only exception from these observations and the cases 1-4 occurs during the workdays 138-140 and is discussed as fifth case in section 0. Note that during that period the Ap values are > the median Ap value.

5.2.2. Case 1: No total fluid losses, maximum number of seismic events

In Case 1, a number of eleven, three, and one seismic events occur (3, 2, 1 with magnitudes M>1) on workday 161, 162, and 163, respectively. The Ap values range from 1.5 to 4.5 during the workdays 157 to 160 and from 9.6 to 14.3 during the workdays 161 to 163. The changes in apparent resistivity and phase of the transfer functions over time are shown in comparison to the reference for the XY and YX components in Fig. 13. Due to the above-mentioned lag in data, MT data are available only for the workdays 156-157, 159-160 and 162-163. For the workdays 159-160, resistivity decreases with respect to the reference are observed between 0.1 and 20 s with minima of 0.1 Ωm and < 0.1 Ωm is observed at 0.17 s and 0.37 s on the XY- and YX components, respectively. This decrease nearly disappears at the workdays 162-163. The remaining offset is shifted towards larger periods. Apart from an increase in uncertainty and decrease in smoothness during the workdays 159-160, the phase follows the reference curve in the XY-component. Changes are significantly more prominent in the YX-component and at periods > 2 s.

5.2.3. Case 2: Total fluid losses, minimum number of seismic events

Case 2 refers to the workdays 112-115 during which total fluid losses of 50 L/s occurred when the well reached a depth of about 4188 m TVD after 30 hours. Minor seismicity (three events of M < 1.2) occurred during workday 113 and 115. The geomagnetic activity is continuously low with a minimum Ap value of 0.9 on workday 116. The apparent resistivity and phase of these workdays (Fig. 14) reveal a resistivity drop to 0.2 Ωm between 4-8 s with respect to the reference that occurs mainly in the YX-components. The phase is characterized by an increase in uncertainty at the same period range. Note that the difference to the reference is comparable to the workdays 156-157 and 162-163, in which no fluid losses occurs (Fig. 13). The reference curve is fully recovered by workday 116 (Fig. 12).

5.2.4. Case 3: No fluid losses, maximum magnitude induced seismicity

This interval is characterized by events with the maximum magnitudes of 1.6 and 1.3 on the workdays 133 and 136, respectively. Note that fluid losses terminate on workday 132. The strong geomagnetic field activity is characterized by Ap values between 11.8 and 23.2. The electromagnetic response of the subsurface in comparison to the reference is presented in Fig. 15. During the workdays 133-134 with the maximum magnitude event, no significant change with respect to the reference is observed. Changes develop at workdays 134-135 and reach a minimum of apparent resistivity of about 0.2 and 0.6 Ωm for the XY- and YX-components at periods of 0.2 to 4 s during the workdays 135-136. The reference is recovered during the workdays 136-137, when the seismicity is ongoing and comes to an end.

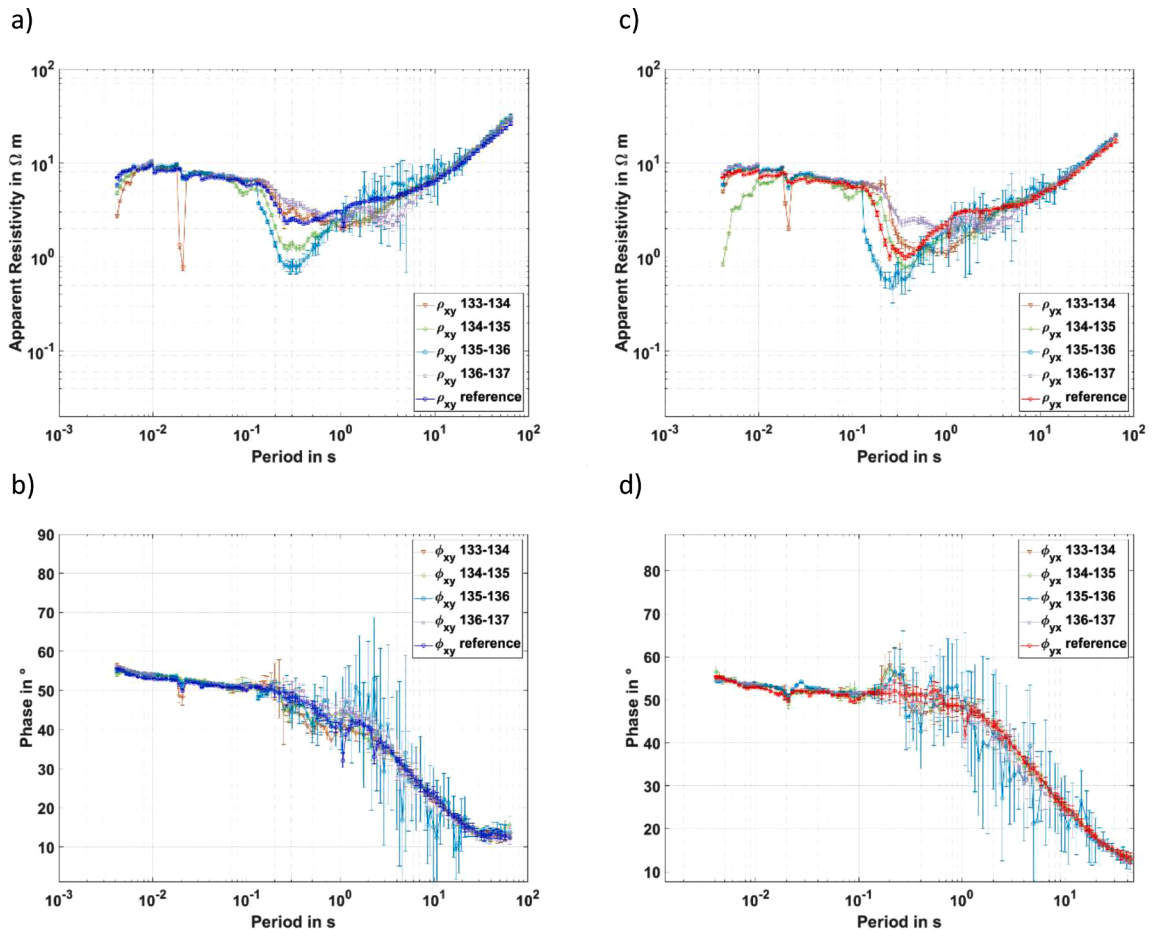

Fig. 15. Transfer functions of the workdays 133-137 during an interval of seismicity with maximum magnitudes for the XY-component with a) apparent resistivity, and b) phase, as well as the YX-component with c) apparent resistivity, and d) phases.

Highest uncertainties in the phase are recorded during the workdays 135-136 in the period range of 0.6-20 s. Besides the related scattering of workday 135-136, the trend of decreasing phase from the reference days is maintained for all workday pairs between 133 and 137.

5.2.5. Case 4: Contemporaneous fluid losses and induced seismicity

This period is characterized by total fluid losses during the workdays 128-132 and continuous induced seismicity during the workdays 126-130 with a peak frequency of four events and a maximum magnitude of 1.4 on workday 127 (Fig. 16). Note that before workdays 126-127 with no fluid losses, a period of four days is characterized by fluid losses. During the workdays 126-129, the geomagnetic activity reveals Ap values below the Ap median value. The resistivity distribution with period between workdays 126-130 can be subdivided into three different characteristic phases for the XY-component:

1) Between workdays 126-128 (comparably low seismicity), a significant minimum of apparent resistivity of 0.1-0.2 Ωm between 0.15 and 1 s, followed by a secondary minimum of about 0.3-1 Ωm between 2 and 7-8 s are observed. Note that both, but in particular the secondary minimum are more prominent at workdays 127-128.
2) With the onset of more prominent seismicity in frequency and magnitudes (workdays 128-129), the minimum of apparent resistivity between 0.15 and 1 s reduces to > 1 Ωm, while the "secondary minimum" remains at values < 1 Ωm.
3) With peak in seismicity during the workdays 129-130, the apparent resistivity distribution of the reference is nearly recovered.

The changes in apparent resistivity in the YX-component reveal one broad minimum of the same range during the workdays 126-127, and two similarly distinguished peaks from workdays 127-128. While in the XY-component the minima disappeared from workdays 129-130, in the YX-component the minimum at 0.1-1 s persists. Comparable to the cases 1 and 2, the phase follows the reference and during workdays revealing apparent resistivity decreases, it is characterized by increase in uncertainty and scattering.

5.2.6. Case 5: Regional seismicity

After the seismic event with a magnitude $M_L < 1$ on workday 138, no local seismicity or fluid losses are observed during the workdays 139-141. The geomagnetic activity is low between workdays 140 and 141. The MT monitoring results reveal a decrease in apparent resistivity on both components starting from the workdays 137-138 comparable to the decrease in case 1 (Fig. 17 a-b and e-f). The data from the workdays 138-140 are characterized by largest uncertainties and strongest scattering of the apparent resistivity and phase values the entire survey (Fig. 1 c-d and g-h). A first improvement is observed in the phase during workdays 140-141. Uncertainties and scattering recovers to values comparable to the observations in the cases 1-4 at workdays 141-142 (Fig. 17 a-b and e-f). The resistivity minimum persists during these workdays. Reference values are recovered during workdays 142-143 when a cluster of seismic events characterizes the processes in the reservoir.

During this period, the SIL seismic network registered several seismic events in the vicinity of the well. A number of events occur close to the bottom hole depth of RN15/IDDP-2. This includes the $M_L = 1.45$ event close to the well at 5'053 m TVD on workday 138. More events occur at the same day at distances of up to 60 km east from the borehole with M_L up to 1.67 at 3'564 m TVD. Deeper seismic events of M_L of 1.25-1.29

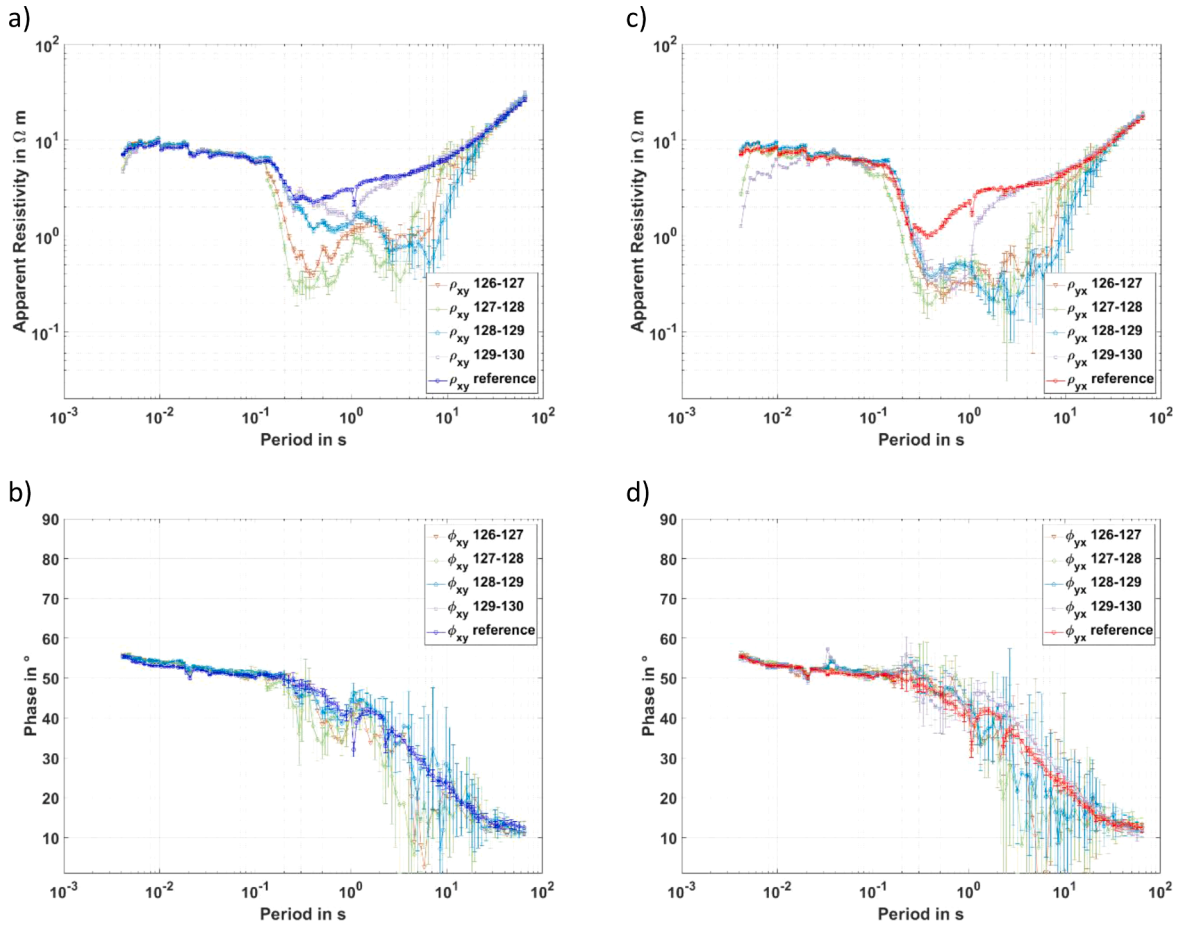

Fig. 16. Transfer functions of the workdays 126-130 during total fluid loss for the XY-component with a) apparent resistivity, and b) phase, as well as the YX-component with c) apparent resistivity, and d) phases.

occur on the workday 140 at TVDs of 7'180 and 10'445 m up to about 60 km east of the borehole. Similarly, to workday 138, also the events on workday 142 are accompanied by a number of events of similar and larger magnitude at this about 60 km distance to the east in a depth range of about 2-5.5 km TVD.

5.3. Comparison of resistivity minima with precipitation

In Fig. 18, we compare the minima of apparent resistivity in the dead band to the precipitation data. The daily precipitation ranges from 0 to 23 mm. Highest precipitation is observed during workdays 127, 138, 148, 157 and 166.The resulting R^2 values of 0.0763 and 0.0327 for the XY and YX components, respectively, do not indicate any significant correlation.

5.4. Comparison of resistivity minima with the geomagnetic activity

To assess the influence of low magnetic activity on the magnetotelluric signal and thus the deduced apparent resistivity in the subsurface, we present a comparison between the A_p value and the apparent resistivity (YX-component) in Fig. 19. Low magnetic activity is defined by Ap values below the median value of Ap = 5 over the entire monitoring period. The apparent resistivity and the Ap values are calculated over 48 hours and shown in 24-hour windows.Although correlation coefficients between the resistivity minima and Ap values are very low (R^2 values of 0.033 for XY and 0.0621 for YX), most of the extreme resistivity minima (more than one order of magnitude lower compared to the reference) occur in periods of low magnetic activity except for the days 132-133, 134-135, 138-139 and 143-144. Except from the workdays 159-160, the extreme resistivity minima do not correspond to the local minima in Ap value. Furthermore, we observe a number of workdays (156-157, 129-130, 137-138) during low geomagnetic activity periods in which no minima are observed.

5.5. Estimate of resistivity changes by extensive fluid losses

To assess possible changes in electric resistivity during extensive fluid losses (Fig. 4), a simple forward model is proposed. Major fluid losses with an electric resistivity of 0.66 Ωm occur in the depth range between 2'900 and 3'300 m. At this depth, a porosity of 10% is observed (Weisenberger et al. 2017).

In the first step, we compare the 1-D inversion of MT measurements at GUN from workday 79 (28/10/2016) to the resistivity distribution with depth from 3-D inversion (see Fig. 2; (Karlsdóttir and Vilhjálmsson 2016) and resistivity logs (HS Orka hf 2017) from the respective depth range (Fig. 20). The determinant was inverted using a Levenberg-Marquardt scheme. Note that the 1-D inversion reveals the general low resistivity zone down to < 2'000 m depth that is characteristic for the area (Fig. 2). At GUN in the 3-D inversion this zone appears to be separated in two distinct layers 200-300 m and 900-2'000 m. This separation is not depicted in the 1-D inversion. No indication of this low resistivity is found in the transfer function of GUN neither. We suspect that it results from the TEM data that are included in the 3-D inversion, but not in our 1-D inversion. Furthermore, in the zone of high fluid losses, the 1-D inversion seems to underestimate the general resistivity provided by logging. However, resistivity logging reveals a number of zones with resistivities that are reduced by up to one order of magnitude with respect to the matrix resistivity, i.e. about 100-200 Ωm.

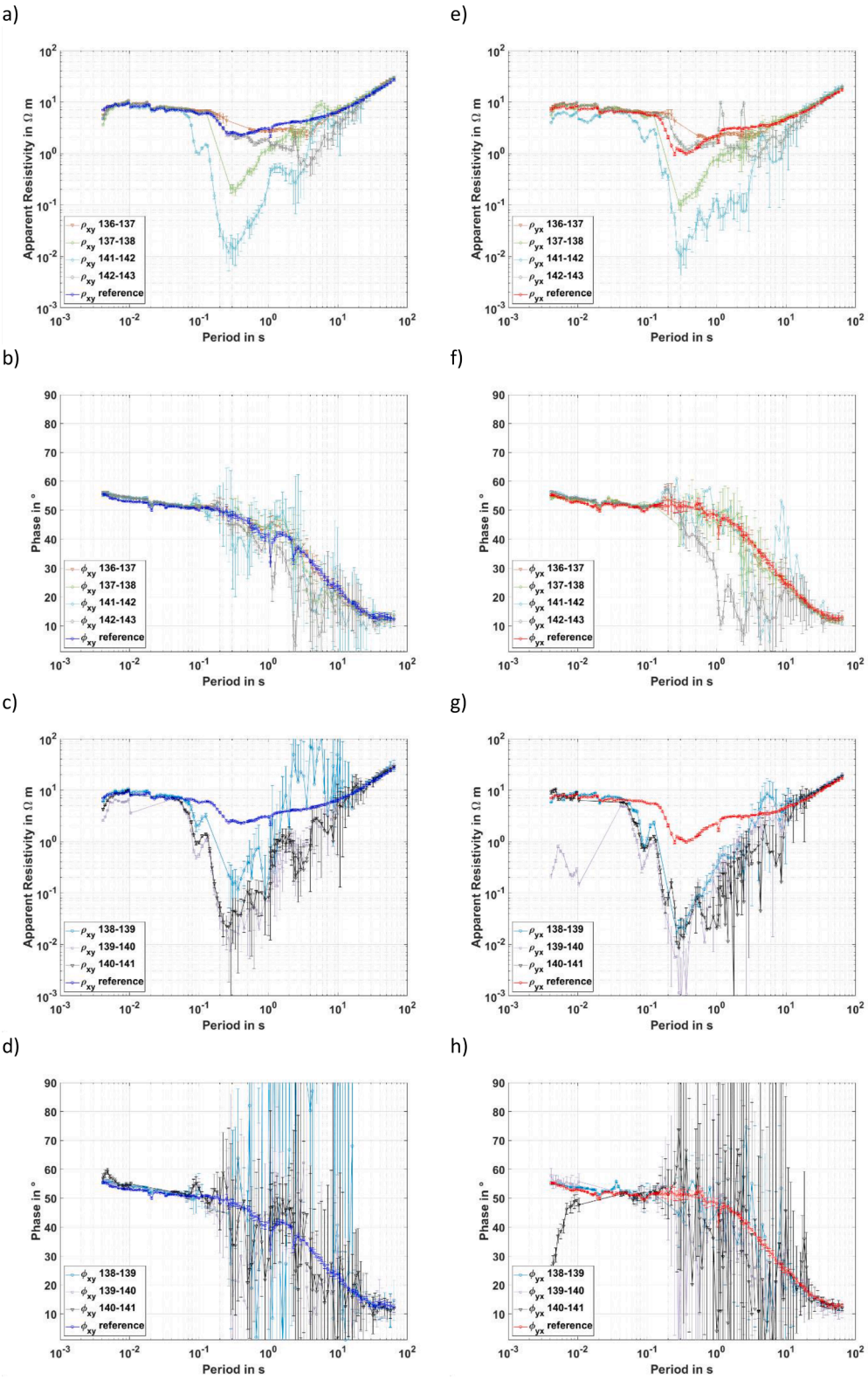

Fig. 17. Transfer functions of the workdays 136-143 during total fluid loss for the XY-component with a)-b) apparent resistivity, and c)-d) phase, as well as the YX-component with e)-f) apparent resistivity, and g)-h) phases.

The thickness of these zones of reduced resistivity range between 5 and < 20 m. These zones sum up to about 40 m thickness and provide pathways for the massive fluid losses during drilling. The overall volume of the fluid losses during drilling is about 91'627 m^3, resulting in a freshwater lens with a radius of about 27 m. Against this background, we add to the resistivity distribution with depth resulting from the 1-D inversion a layer of 40 m with a by about one order of magnitude reduced resistivity (namely 0.66 Ωm) in order to investigate the effect of fluid losses on the MT data (dashed line in Fig. 20).

Fig. 21 reveals expected low differences of 1 Ωm (and 3° in the

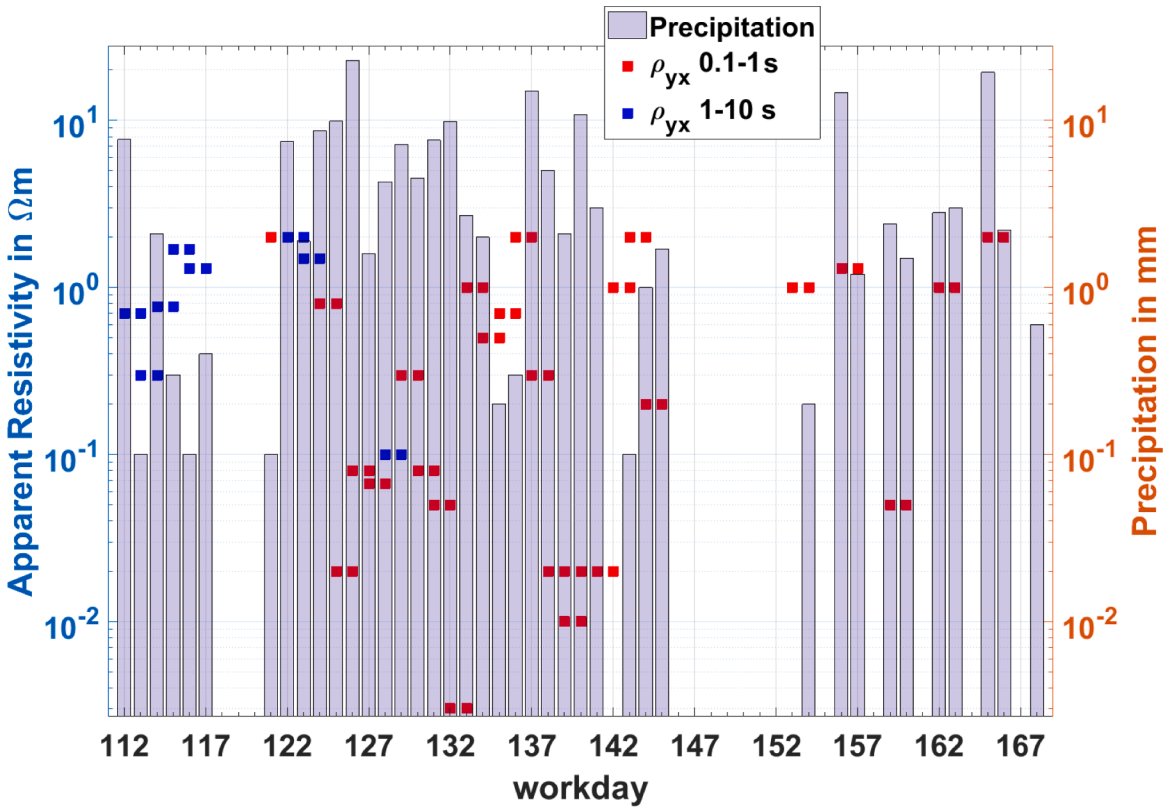

Fig. 18. Precipitation data in mm with the apparent resistivity minima in the so-called dead band (1-10 s) of the XY and the YX components (Icelandic Meteorological Office 2017).

phase) between the transfer function of the measured data at GUN and the results from forward modelling of the resistivity distribution with depth of the 1-D inversion with the additional resistivity low resulting from the fluid losses. Note that given the small radius of the freshwater lens, the resulting changes even overestimate the effect.

5.6. Temporal changes in the phase tensor

The residual phase tensors are shown for the individual workdays in Fig. 22 and compared to the geomagnetic activity. The phase tensors residuals are calculated after Caldwell et al.; Peacock et al. (2004; 2013) by subtracting the individual workdays from the reference workdays 46-47. Thus, scalar differences are represented by circular shape, while directional dependent changes result in an ellipsoidal shape (Peacock et al., 2013). Phase tensor residuals are normalized to the reference (workdays 46-47) and determined in 48h windows.

Generally, the geometric mean (color code in Fig. 22) reveals differences of up to 30-40 % with respect to the reference. For periods < 0.05 s, the phase tensors show only slight differences to the reference. During the workdays 112-113, 126-129 and 142-143 changes between 50-65 % are observed in the period range of 4-8 s. The phase tensors of the workdays 139-143 reveal by far the largest expansion between the periods 0.1-16 s and the highest percent changes with values between 60-100 %.

The residual phase tensors predominantly show a circular shape; whenever shape becomes ellipsoidal, its predominant orientation is E-W. This is consistent with the observations in the cases 1-5 that show more pronounced resistivity minima in the YX-components compared to the XY-components. This summary shows the highest percent changes values in intervals of low geomagnetic activity but there are also changes of up to 50 % in intervals of high geomagnetic activity.

6. Discussion and conclusion

First, note that no consistent anthropogenic noise source, which correlates with the intervals and frequencies of the observations in the transfer functions, i.e., the decrease in apparent resistivity, could be detected neither in the time series nor in the power spectra with methods applied in this study. High-frequency anthropogenic noise was eliminated by filtering and decimation. In addition, the time-frequency analysis show that only the electric time series are affected by a periodic signal. This seems to be linked to tidal activity. With a frequency of $2.32 \bullet 10^{-5}$ Hz, however, it is beyond frequency range of interest (10^{-3}-10^{2} Hz).

This study started with the ambition to relate external geomagnetic, hydraulic or seismic processes to the origin of the low resistivity anomalies. In this respect, three type transfer functions are obtained during the MT monitoring of the deepening period of RN15/IDDP-2. All three reveal enhanced uncertainties in the phase in the period intervals of 3-20 s. The type functions are discriminated by their distribution of apparent resistivity with period. They occur temporarily related to geomagnetic, hydraulic and seismic observations.

- No significant variation with respect to the reference workdays 46-47 are observed during workdays in which neither fluid losses nor significant induced seismicity observed, or during workdays in which no fluid losses but seismicity occurs that is significant either in magnitude or in the number of events. Such transfer functions are observed during low and high geomagnetic activity.
- Significant minima of resistivity between periods of 0.15 and 1 s with minimum resistivity values in the order of 0.1 Ωm and smaller occur during workdays preceding significant induced seismic events of either relatively large magnitude or number of events. These minima are slightly more pronounced in the YX-component. Two periods of the extreme minima fall into periods of low geomagnetic activity

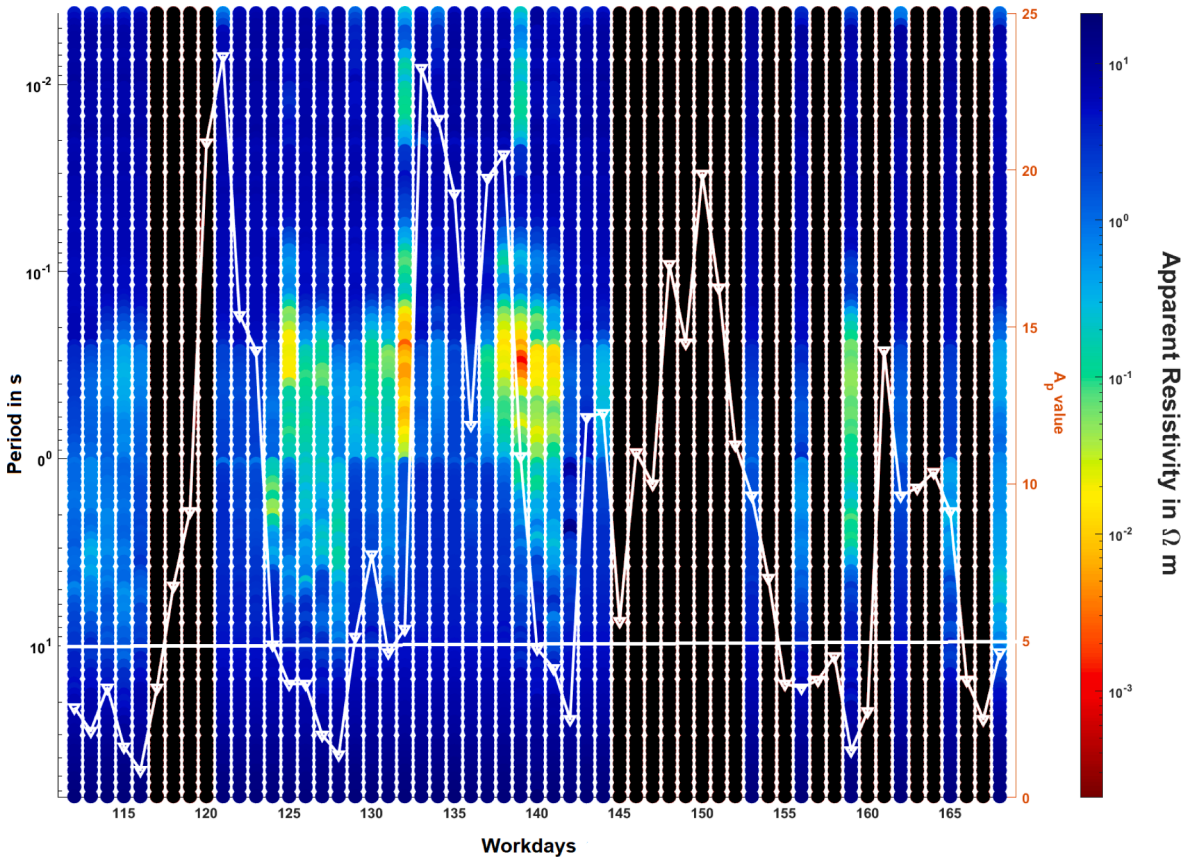

Fig. 19. The geomagnetic activity as Ap value (GFZ German Research Centre For Geosciences 2020) with the apparent resistivity values (YX component). Both parameters are calculated over 48 hours and shown with a 24-hour window. The white line shows the median value of Ap=5. The black columns are days without MT data.

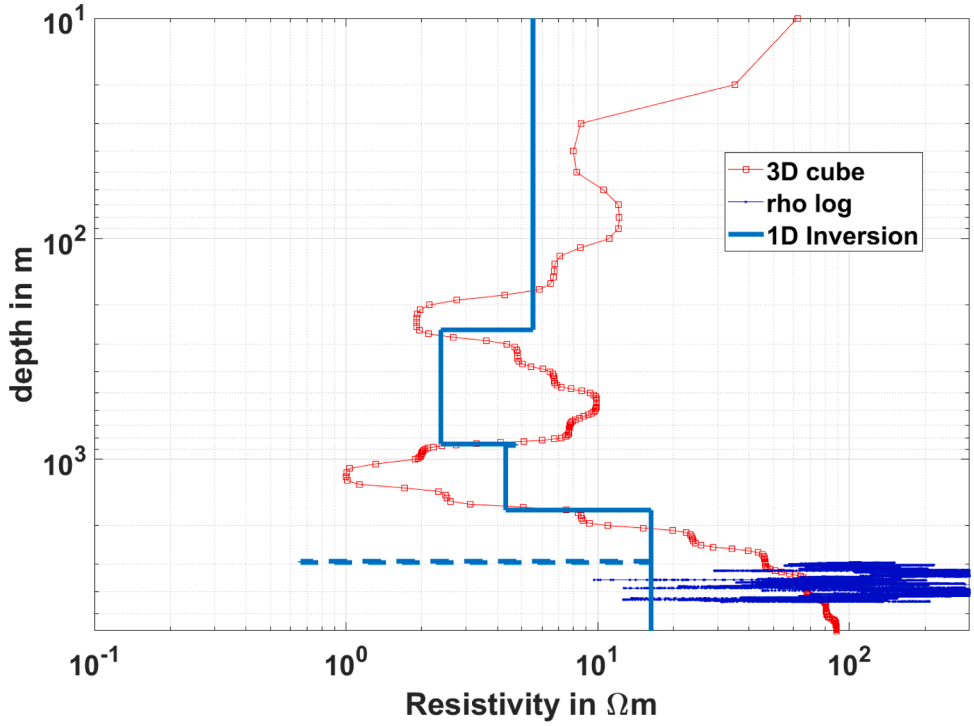

Fig. 20. Resistivity distributions of the 3D model, the 1D inversion, the forward model and the resistivity log of the well RN-15/IDDP-2, (HS Orka hf 2017).

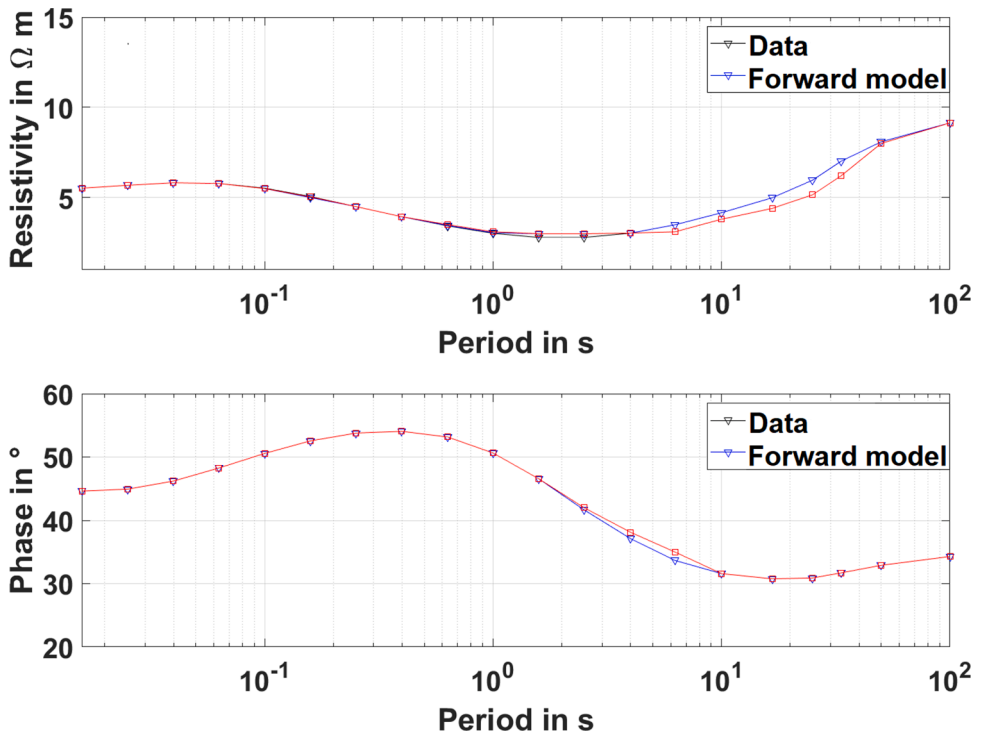

Fig. 21. Obtained transfer function of the layered model (triangle) and the forward model with the resistivities (a) and the corresponding phases (b).

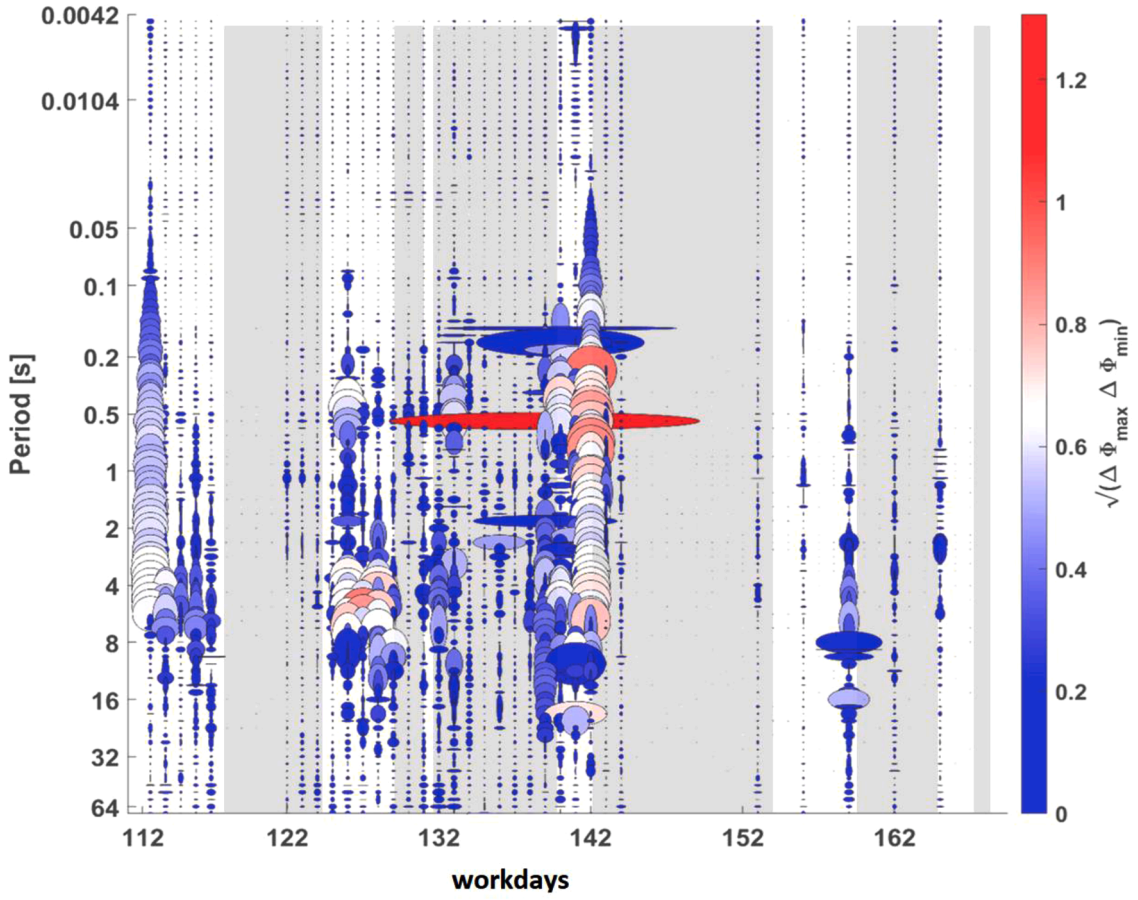

Fig. 22. Overview of the calculated phase tensor residuals and intervals of geomagnetic activity (Ap values) above (grey) and below (white) the Ap median. The phase tensors residuals are calculated between the reference and the phase tensors of the corresponding workdays (Peacock et al. 2013).

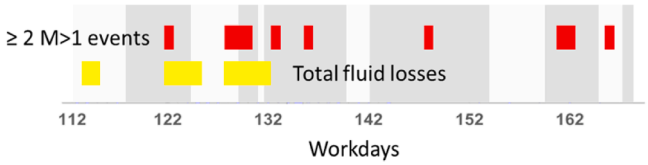

Fig. 23. Summary of the temporal coincidence of high geomagnetic activity (grey), major seismic activity (red), and periods of total fluid losses (yellow) for the workdays 112-169.

Table 4
New summary of the tectonic boundary condition and electromagnetic observations during injection experiments in EGS wells (Peacock et al. 2012; Peacock et al. 2013; Didana et al. 2017; Abdelfettah et al. 2018; Baujard et al. 2017).

Orientation of \ Site	Paralana	Habanero	Rittershoffen	RN15/IDDP-2
SHmax	N110°E	N82±5°E	N170°E	N30°E
Seismic cloud	NNE-SSW, NE-SW	Horizontally extended with tendency to N-S, NNE-SSW orientation	n/a	Scattered with no specific induced swarms.
Geoelectric strike	N9°E	N50°E	N-S	N5°E
Residual phase tensor during injection	N-S, NNE-SSW	N-S	N170°E	isotropic to E-W
Significant resistivity minima component	XY ∥ N-S	XY ∥ N-S	YX ∥ E-W	XY ∥ N-S and YX ∥ E-W
Approximate frequency range of resistivity minima	2-20 s	17-34 s	8-20 s	0.2-20 s and 4-20 s

(workdays 125-126 and 159.160), while the other two coincide with transitional periods (workdays132-133 and 139-140).

- During intervals of total fluid losses, secondary minima between periods of 4-8 s with a minimum value of about 1 Ωm are observed. Note that all minima in this period range coincide with periods of low geomagnetic activity. They may however also occur during workdays without fluid losses.

Although major resistivity minima occur mostly during periods of low geomagnetic activity, this trend is not fully explaining the occurrence and absence of such minima. In Fig. 23 we present a summary of the temporal coincidences between these processes, to identify workdays with optimal constellations of high geomagnetic activity and hydraulic or seismic processes. Optimal constellations at the workdays 122, 148 and 161 lack of data before the seismic events occur. Furthermore, the simplified modeling showed that also the fluid losses cannot explain the amplitude of the observed resistivity decreases. The remaining optimal constellations at workdays 133 and 136 reveal an overlap with total fluid losses prior to workday 133 and an important resistivity decrease at short periods (< 1 s; Fig. 15).

Against the background of this low number of optimal constellations, an attribution of this "noise" to geogenic processes is not conclusive. In comparison to earlier MT monitoring surveys mentioned in section 0, the following differences and similarities are observed (Table 4). Note that a detailed analysis of the Habanero site with regard to the transfer functions is not provided in the literature. Therefore, our discussion focuses on the comparison with the Paralana and Rittershoffen sites.

1) With two exceptions, the resistivity minima occur in rather similar period ranges between 2, 4 and 8 to 20 s at Paralana, RN15/IDDP-2 (secondary minima), and Rittershoffen, respectively. Minima at the period range > 0.2 s are observed for the first time at RN15/IDDP-2. The minima at Habanero are observed at longer periods of 17-34 s.
2) In contrast to the Paralana, Habanero, and Rittershoffen sites, at the RN15/IDDP-2 well significant resistivity minima are observed nearly equally distributed on both, XY and YX components with slightly smaller values of apparent resistivities in the YX component.
3) Although revealing similar geoelectric strikes and residual phase tensor orientations during injection, the directional occurrence of the resistivity minima differs strongly between Paralana, Rittershoffen, and RN15/IDDP-2. While at Paralana resistivity minima occur in the component parallel to the strike and residual phase tensor, at Rittershoffen, it occurs perpendicular to this direction and at RN15/IDDP-2 it even occurs on both directions.
4) The parallelism of the respective components with apparent resistivity minima are observed with the orientation of Shmin for Paralana, Habanero, and Rittershoffen and partly with the orientation of the seismic cloud at Paralana. Note that at Rittershoffen no seismicity was observed. However, the significant minima in apparent resistivity occur perpendicular to the major fault zones (Baujard et al. 2017). At RN15/IDDP-2, the seismic cloud is scattered and follows no specific induced swarm. The Shmin (N120°E) is oriented between the two components.

In conclusion, this study enlarges the observation of changes in the electromagnetic field in the subsurface induced by measures during reservoir engineering or even natural seismicity with a new dataset including a continuous magnetotelluric monitoring over two months as well as results from seismic monitoring and the related hydraulic data of the RN15/IDDP-2 well. This new dataset shows a temporal relation between decreasing apparent resistivity that is considered induced noise and

1) the geomagnetic field activity,
2) the fluid losses up to 60 L/s, as well as
3) mechanic processes occurring in the reservoir prior to clusters of induced seismicity on the other hand.

None of these fully explains the resistivity minima neither in the period range of 0.15-1 s, nor in the range of 4-8 s. The temporal occurrence of changes in resistivity hints to a relation between the resistivity decrease and processes induced in the reservoir. We consider these changes in the transfer functions as noise that is induced in the subsurface either directly caused by processes associated to the fluid injection or indirectly by inducing seismicity. However, against the frequent temporal coincidence with periods of low geomagnetic activity, the full physical meaning of our values of apparent resistivity and frequency remains a matter of debate.

Declaration of Competing Interest

The authors declare that they have no known competing financial interests or personal relationships that could have appeared to influence the work reported in this paper.

Acknowledgements

The IDDP-2 was funded by HS Orka, Landsvirkjun, Orkuveita Reykjavíkur, and the National Energy Authority in Iceland, together with Equinor (Norway). The IDDP-2 and our project have received funding from the DEEPEGS project, European Union's HORIZON 2020 research and innovation program under grant agreement No 690771. We would like to thank HS ORKA for providing access to the site as well as 3-D MT dataset over the Reykjanes geothermal field and the seismic and hydraulic data acquired during the monitoring period. We are very grateful to Steinþór Níelsson, Stephan Audunn Stefansson, Ragna Karlsdóttir and Knútur Árnason from the Iceland Geosurvey (ISOR) for their conceptual and logistical support before and during the surveys. We would like also to thank Mathieu Darnet, Nicolas Coppo and Pierre Wawrzyniak of the French BRGM for their support during the field work and data processing.

References

Abdelfettah, Y., Sailhac, P., Larnier, H., Matthey, P.-D., Schill, E., 2018. Continuous and time-lapse magnetotelluric monitoring of low volume injection at Rittershoffen geothermal project, northern Alsace – France. Geothermics 71. https://doi.org/10.1016/j.geothermics.2017.08.004, 1–11.

Albaric, J., Oye, V., Langet, N., Hasting, M., Lecomte, I., Iranpour, K., et al., 2014. Monitoring of induced seismicity during the first geothermal reservoir stimulation at Paralana, Australia. Geothermics 52, 120–131. https://doi.org/10.1016/j.geothermics.2013.10.013.

Baisch, S., Weidler, R., Voros, R., Wyborn, D., Graaf, L.de, 2006. Induced seismicity during the stimulation of a geothermal HFR reservoir in the Cooper Basin, Australia. Bull. Seismol. Soc. Am. 96 (6), 2242–2256. https://doi.org/10.1785/0120050255.

Baisch, Stefan, Vörös, Robert, Rothert, Elmar, Stang, Henrik, Jung, Reinhard, Schellschmidt, Rüdiger, 2010. A numerical model for fluid injection induced seismicity at Soultz-sous-Forêts. Int. J. Rock Mech. Min. Sci. 47 (3), 405–413. https://doi.org/10.1016/j.ijrmms.2009.10.001.

Baujard, C., Genter, A., Dalmais, E., Maurer, V., Hehn, R., Rosillette, R., et al., 2017. Hydrothermal characterization of wells GRT-1 and GRT-2 in Rittershoffen, France: Implications on the understanding of natural flow systems in the rhine graben. Geothermics 65, 255–268. https://doi.org/10.1016/j.geothermics.2016.11.001.

Becken, M., Burkhardt, H., 2004. An ellipticity criterion in magnetotelluric tensor analysis. Geophys. J. Int. 159 (1), 69–82. https://doi.org/10.1111/j.1365-246X.2004.02376.x.

Chave, Alan D., Thomson, David J., 2003. A bounded influence regression estimator based on the statistics of the hat matrix. J. R. Stat. Soc. C 52 (3), 307–322. https://doi.org/10.1111/1467-9876.00406.

Chave, Alan D., Thomson, David J., 2004. Bounded influence magnetotelluric response function estimation. Geophys. J. Int. 157 (3), 988–1006. https://doi.org/10.1111/j.1365-246X.2004.02203.x.

Chave, Alan Dana, Jones, Alan G, 2012. The Magnetotelluric Method. Theory and practice. Cambridge University Press, New York.

Clarke, J., Gamble, T.D., Goubau, W.M., KOCH, R.H., MIRACKY, R.F., 1983. Remote-reference magnetotellurics: equipment and procedures*. Geophys. Prospect. 31 (1), 149–170. https://doi.org/10.1111/j.1365-2478.1983.tb01047.x.

Cuenot, Nicolas, Dorbath, Catherine, Dorbath, Louis, 2008. Analysis of the Microseismicity Induced by Fluid Injections at the EGS Site of Soultz-sous-Forêts (Alsace, France): implications for the characterization of the geothermal reservoir properties. Pure Appl. Geophys. 165 (5), 797–828. https://doi.org/10.1007/s00024-008-0335-7.

Darnet, M., 2004. On the origins of self-potential (SP) anomalies induced by water injections into geothermal reservoirs. Geophys. Res. Lett. 31 (19), 226. https://doi.org/10.1029/2004GL020922.

Darnet, M., Wawrzyniak, P., Coppo, N., Nielsson, S., Schill, E., Fridleifsson, G.Ó., 2020. Monitoring geothermal reservoir developments with the controlled-source electromagnetic method — a calibration study on the Reykjanes geothermal field. J. Volcanol. Geotherm. Res. 391, 106437 https://doi.org/10.1016/j.jvolgeores.2018.08.015.

Didana, Yohannes Lemma, Heinson, Graham, Thiel, Stephan, Krieger, Lars, 2017. Magnetotelluric monitoring of permeability enhancement at enhanced geothermal system project. Geothermics 66, 23–38. https://doi.org/10.1016/j.geothermics.2016.11.005.

Freund, Friedemann, 2011. Pre-earthquake signals: underlying physical processes. J. Asian Earth Sci. 41 (4-5), 383–400. https://doi.org/10.1016/j.jseaes.2010.03.009.

Friðleifsson, G.Ó., Sigurdsson, Ó., Þorbjörnsson, D., Karlsdóttir, R., Gíslason, Þ., Albertsson, A., Elders, W.A., 2014. Preparation for drilling well IDDP-2 at Reykjanes. Geothermics 49, 119–126. https://doi.org/10.1016/j.geothermics.2013.05.006.

Friðleifsson, Guðmundur Ómar; Elders, Wilfred A.; ZierenbergRobert; Weisenberger, Tobias B.; Harðarson, Björn S.; Stefánsson, Ari et al. (2017): IDDP-2-Completion-websites-IDDP-DEEPEGS-5: scientific drilling, (23, 1-12.).

Gamble, T.D., Goubau, W.M., Clarke, J., 1979. Magnetotellurics with a remote magnetic reference. Geophysics 44 (1), 53–68. https://doi.org/10.1190/1.1440923.

Gershenzon, N., Bambakidis, G., 2001. Modeling of seismo-electromagnetic phenomena. Russ. J. Earth Sci. 3 (4), 247–275. https://doi.org/10.2205/2001ES000058.

GFZ German Research Centre For Geosciences, 2020. Kp Index. Online verfügbar unter. https://www.gfz-potsdam.de/en/kp-index/. zuletzt aktualisiert am 17.07.2020, zuletzt geprüft am 17.07.2020.

Guðnason, E.Á., Ágústsson, K., Gunnarsson, K., Flóvenz, Ó.G., 2015. Seismic Activity on Reykjanes December 2014 – November 2015. Iceland GeoSurvey 2015.

Guðnason, E.Á., Ágústsson, K., Gunnarsson, K., Flóvenz, Ó.G., 2016. Seismic Activity on Reykjanes December 2015 – November 2016. Iceland GeoSurvey 2016.

Häring, Markus O., Schanz, Ulrich, Ladner, Florentin, Dyer, Ben, C., 2008. Characterisation of the Basel 1 enhanced geothermal system. Geothermics 37 (5), 469–495. https://doi.org/10.1016/j.geothermics.2008.06.002.

HS Orka hf (2017): DEEPEGS. Project file. Hydraulic Data IDDP-2/RN-15.

Icelandic Meteorological Office (2017): Seismic catalogue of the SIL regional network 2016 and 2017.

Johannesson, H., Sæmundsson, K., 2009. Geological map of Iceland. Náttúrufræðistofnun Íslands - Icelandic Institute of Natural History. 2009.

Junge, Andreas, 1996. Characterization of and correction for cultural noise. Surv. Geophys. 17 (4), 361–391. https://doi.org/10.1007/BF01901639.

Karlsdóttir, Ragna, Vilhjálmsson, Arnar Már, 2016. Reykjanes – Sandvík 3D Inversion of MT Data. ISOR.

Keiding, M., Lund, B., Árnadóttir, T., 2009. Earthquakes, stress, and strain along an obliquely divergent plate boundary: Reykjanes Peninsula, southwest Iceland. J. Geophys. Res. 114 (B9), T17. https://doi.org/10.1029/2008JB006253.

Marquis, Guy, Darnet, Mathieu, Sailhac, Pascal, Singh, A.K., Gérard, André, 2002. Surface electric variations induced by deep hydraulic stimulation: an example from the Soultz HDR site. Geophys. Res. Lett. 29 (14) https://doi.org/10.1029/2002GL015046, 7-1-7-4.

Ohta, K., Izutsu, J., Schekotov, A., Hayakawa, M., 2013. The ULF/ELF electromagnetic radiation before the 11 March 2011 Japanese earthquake. Radio Sci. 48 (5), 589–596. https://doi.org/10.1002/rds.20064.

Peacock, J.R., Thiel, S., Reid, P., Heinson, G., 2012. Magnetotelluric monitoring of a fluid injection. Example from an enhanced geothermal system. Geophys. Res. Lett. 39 (18), 165. https://doi.org/10.1029/2012GL053080.

Peacock, Jared R., Thiel, Stephan;, Heinson, Graham S., Reid, Peter, 2013. Time-lapse magnetotelluric monitoring of an enhanced geothermal system. Geophysics 78 (3), B121–B130. https://doi.org/10.1190/geo2012-0275.1.

Petraki, E., Nikolopoulos, D., Nomicos, C., Stonham, J., Cantzos, D., Yannakopoulos, P., Kottou, 2015. Electromagnetic pre-earthquake precursors: mechanisms, data and models-a review. J. Earth Sci. Clim. Change 06 (01). https://doi.org/10.4172/2157-7617.1000250.

Ritter, Oliver, Muñoz, G., Weckmann, Ute, Klose, Reinhard, Rulff, Paula, Rettig, St., et al., 2015. A Permanent Magnetotelluric Remote Reference Station in Wittstock, Germany.

Schill, E., Genter, A., Cuenot, N., Kohl, T., 2017. Hydraulic performance history at the Soultz EGS reservoirs from stimulation and long-term circulation tests. Geothermics 70, 110–124. https://doi.org/10.1016/j.geothermics.2017.06.003.

Schoenball, Martin, Dorbath, Louis, Gaucher, Emmanuel, Wellmann, J.Florian, Kohl, Thomas, 2014. Change of stress regime during geothermal reservoir stimulation. Geophys. Res. Lett. 41 (4), 1163–1170. https://doi.org/10.1002/2013GL058514.

Sigurðsson, Ómar, 2018. Stimulation of the RN-15/IDDP-2 well at Reykjanes in an attempt to create an EGS system. Deliverable: D6.5 DEEPEGS.

Weisenberger, Tobias B., Harðarson, Björn, S., Kästner, F., Gunnarsdóttir, Sveinborg, H., Tulinius, Helga;, Guðmundsdóttir, V., et al., 2017. Deliverable: D6.4 Well Report – RN-15/IDDP-2. Drilling in Reykjanes - Phases 4 and 5 from 3000 to 4659 m.

Welch, P.D., 1967. The use of fast Fourier transform for the estimation of power spectra: a method based on time averaging over short modified periodograms. IEEE Trans. Audio Electroacoust. 15 (2).